Research Article Vol. 26, No. 7 | 2 Apr 2018 | OPTICS EXPRESS 8125
Optics EXPRESS

# Space-borne profiling of atmospheric thermodynamic variables with Raman lidar: performance simulations

PAOLO DI GIROLAMO,[1,*] ANDREAS BEHRENDT,[2] VOLKER WULFMEYER[2]

[1]*Scuola di Ingegneria, Università degli Studi della Basilicata, Viale dell'Ateneo Lucano n. 10, 85100 Potenza, Italy*
[2]*Institut für Physik und Meteorologie, Universität Hohenheim, Garbenstrasse 30, D-70599 Stuttgart, Germany*
**paolo.digirolamo@unibas.it*

**Abstract:** The performance of a space-borne water vapour and temperature lidar exploiting the vibrational and pure rotational Raman techniques in the ultraviolet is simulated. This paper discusses simulations under a variety of environmental and climate scenarios. Simulations demonstrate the capability of Raman lidars deployed on-board low-Earth-orbit satellites to provide global-scale water vapour mixing ratio and temperature measurements in the lower to middle troposphere, with accuracies exceeding most observational requirements for numerical weather prediction (NWP) and climate research applications. These performances are especially attractive for measurements in the low troposphere in order to close the most critical gaps in the current earth observation system. In all climate zones, considering vertical and horizontal resolutions of 200 m and 50 km, respectively, mean water vapour mixing ratio profiling precision from the surface up to an altitude of 4 km is simulated to be 10%, while temperature profiling precision is simulated to be 0.40-0.75 K in the altitude interval up to 15 km. Performances in the presence of clouds are also simulated. Measurements are possible above and below cirrus clouds with an optical thickness of 0.3. This combination of accuracy and vertical resolution cannot be achieved with any other space borne remote sensing technique and will provide a breakthrough in our knowledge of global and regional water and energy cycles, as well as in the quality of short- to medium-range weather forecasts. Besides providing a comprehensive set of simulations, this paper also provides an insight into specific possible technological solutions that are proposed for the implementation of a space-borne Raman lidar system. These solutions refer to technological breakthroughs gained during the last decade in the design and development of specific lidar devices and sub-systems, primarily in high-power, high-efficiency solid-state laser sources, low-weight large aperture telescopes, and high-gain, high-quantum efficiency detectors.



**OCIS codes:** (010.0280) Remote sensing and sensors; (280.3640) Lidar; (010.7340) Water; (280.6780) Temperature; (010.1110) Aerosols; (300.6450) Spectroscopy, Raman.

## References and links

1. Intergovernmental Panel on Climate Change, "Climate Change 2013: The physical science basis," in *5th Assessment Report, IPCC WGI AR5*, edited by T. F. Stocker, D. Qin, G.-K. Plattner, M. Tignor, S. K. Allen, J. Boschung, A. Nauels, Y. Xia, V. Bex and P.M. Midgley (Cambridge University, 2013) Cambridge, U. K.
2. Intergovernmental Panel on Climate Change, "Climate Change 2014: Impacts, adaptation, and vulnerability," in *5th Assessment Report, IPCC WGII AR5, Technical Summary*, Coordinating Lead Authors: C. Field, V. Barros, K. Mach, and M. Mastrandrea, available at http://www.ipcc.ch/report/ar5/wg2 (IPCC, 2014), Geneva, Switzerland.
3. Intergovernmental Panel on Climate Change, "Climate Change 2014: Synthesis Report" in *5th Assessment Report, Working Groups I, II and III*, Core Writing Team, R. K. Pachauri and L. A. Meyer (eds.) (IPCC, 2014) Geneva, Switzerland, 151 pp.

#306852 https://doi.org/10.1364/OE.26.008125
Journal © 2018 Received 6 Oct 2017; revised 10 Feb 2018; accepted 11 Feb 2018; published 21 Mar 2018
Corrected: 10 April 2018

Optics EXPRESS


4. D. P. Dee, S. M. Uppala, A. J. Simmons, P. Berrisford, P. Poli, S. Kobayashi, U. Andrae, M. A. Balmaseda, G. Balsamo, P. Bauer, P. Bechtold, A. C. M. Beljaars, L. van de Berg, J. Bidlot, N. Bormann, C. Delsol, R. Dragani, M. Fuentes, A. J. Geer, L. Haimberger, S. B. Healy, H. Hersbach, E. V. Hólm, L. Isaksen, P. Kållberg, M. Köhler, M. Matricardi, A. P. McNally, B. M. Monge-Sanz, J.-J. Morcrette, B.-K. Park, C. Peubey, P. de Rosnay, C. Tavolato, J.-N. Thépaut, and F. Vitart, "The ERA-Interim reanalysis: Configuration and performance of the data assimilation system," Q. J. R. Meteorol. Soc. **137**(656), 553–597 (2011).
5. N. A. Crook, "Sensitivity of moist convection forced by boundary layer processes to low-level thermodynamic fields," Mon. Weather Rev. **124**(8), 1767–1785 (1996).
6. S. Dierer, M. Arpagaus, A. Seifert, E. Avgoustoglou, R. Dumitrache, F. Grazzini, P. Mercogliano, M. Milelli, and K. Starosta, "Deficiencies in quantitative precipitation forecasts: sensitivity studies using the COSMO model," Meteorol. Z. **18**(6), 631–645 (2009).
7. L. Bengtsson, K. I. Hodges, and S. Hagemann, "Sensitivity of the ERA40 reanalysis to the observing system: determination of the global atmospheric circulation from reduced observations," Tellus, Ser. A, Dyn. Meterol. Oceanogr. **56**(5), 456–471 (2004).
8. K. Warrach-Sagi, T. Schwitalla, V. Wulfmeyer, and H.-S. Bauer, "Evaluation of a climate simulation based on the WRF-NOAH model system: precipitation in Germany," Clim. Dyn. **41**(3-4), 755–774 (2013).
9. S. Kotlarski, K. Keuler, O. B. Christensen, A. Colette, M. Déqué, A. Gobiet, K. Goergen, D. Jacob, D. Lüthi, E. van Meijgaard, G. Nikulin, C. Schär, C. Teichmann, R. Vautard, K. Warrach-Sagi, and V. Wulfmeyer, "Regional climate modeling on European scales: a joint standard evaluation of the EURO-CORDEX RCM ensemble," Geosci. Model Dev. **7**(4), 1297–1333 (2014).
10. V. Wulfmeyer, R. M. Hardesty, D. D. Turner, A. Behrendt, M. P. Cadeddu, P. Di Girolamo, P. Schlüssel, J. Van Baelen, and F. Zus, "A review of the remote sensing of lower-tropospheric thermodynamic profiles and its indispensable role for the understanding and the simulation of water and energy cycles," Rev. Geophys. **53**(3), 819–895 (2015).
11. E. R. Kursinski, G. A. Haji, K. R. Hardy, J. T. Schofield, and R. Linfield, "Observing Earth's atmosphere with radio occultation measurements using the Global Positioning System," J. Geophys. Res. **102**(D19), 23429–23465 (1997).
12. S. B. Healy, J. R. Eyre, M. Hamrud, and J.-N. Thépaut, "Assimilating GPS radio occultation measurements with two-dimensional bending angle observation operators," Q. J. R. Meteorol. Soc. **133**(626), 1213–1227 (2007).
13. C. Cardinali and S. Healy, "Impact of GPS radio occultation measurements in the ECMWF system using adjoint-based diagnostics," Q. J. R. Meteorol. Soc. **140**(684), 2315–2320 (2014).
14. P. Poli, S. B. Healy, and D. P. Dee, "Assimilation of Global Positioning System radio occultation data in the ECMWF ERA–Interim reanalysis," Q. J. R. Meteorol. Soc. **136**(653), 1972–1990 (2010).
15. P. Vergados, A. J. Mannucci, and C. O. Ao, "Assessing the performance of GPS radio occultation measurements in retrieving tropospheric humidity in cloudiness: A comparison study with radiosondes, ERA-Interim, and AIRS data sets," J. Geophys. Res. Atmos. **119**(12), 7718–7731 (2014).
16. P. Di Girolamo, A. Behrendt, and V. Wulfmeyer, "Spaceborne profiling of atmospheric temperature and particle extinction with pure rotational Raman Lidar and of relative humidity in combination with differential absorption lidar: performance simulations," Appl. Opt. **45**(11), 2474–2494 (2006).
17. D. N. Whiteman, S. H. Melfi, and R. A. Ferrare, "Raman lidar system for the measurement of water vapor and aerosols in the Earth's atmosphere," Appl. Opt. **31**(16), 3068–3082 (1992).
18. A. Behrendt and J. Reichardt, "Atmospheric temperature profiling in the presence of clouds with a pure rotational Raman lidar by use of an interference-filter-based polychromator," Appl. Opt. **39**(9), 1372–1378 (2000).
19. I. Mattis, A. Ansmann, D. Althausen, V. Jaenisch, U. Wandinger, D. Müller, Y. F. Arshinov, S. M. Bobrovnikov, and I. B. Serikov, "Relative-humidity profiling in the troposphere with a Raman lidar," Appl. Opt. **41**(30), 6451–6462 (2002).
20. A. Behrendt, T. Nakamura, M. Onishi, R. Baumgart, and T. Tsuda, "Combined Raman lidar for the measurement of atmospheric temperature, water vapor, particle extinction coefficient, and particle backscatter coefficient," Appl. Opt. **41**(36), 7657–7666 (2002).
21. A. Behrendt, T. Nakamura, and T. Tsuda, "Combined temperature lidar for measurements in the troposphere, stratosphere, and mesosphere," Appl. Opt. **43**(14), 2930–2939 (2004).
22. A. Behrendt, V. Wulfmeyer, E. Hammann, S. K. Muppa, and S. Pal, "Profiles of second to third order moments of turbulent temperature fluctuations in the convective boundary layer, First measurements with rotational Raman lidar," Atmos. Chem. Phys. **15**(10), 5485–5500 (2015).
23. P. Di Girolamo, R. Marchese, D. N. Whiteman, and B. B. Demoz, "Rotational Raman Lidar measurements of atmospheric temperature in the UV," Geophys. Res. Lett. **31**(1), L01106 (2004).
24. P. Di Girolamo, A. Behrendt, C. Kiemle, V. Wulfmeyer, H. Bauer, D. Summa, A. Dörnbrack, and G. Ehret, "Simulation of satellite water vapour lidar measurements: Performance assessment under real atmospheric conditions," Remote Sens. Environ. **112**(4), 1552–1568 (2008).
25. P. Di Girolamo, D. Summa, and R. Ferretti, "Multiparameter Raman Lidar Measurements for the Characterization of a Dry Stratospheric Intrusion Event," J. Atmos. Ocean. Technol. **26**(9), 1742–1762 (2009).
26. M. Radlach, A. Behrendt, and V. Wulfmeyer, "Scanning rotational Raman lidar at 355 nm for the measurement of tropospheric temperature fields," Atmos. Chem. Phys. **8**(2), 159–169 (2008).

Optics EXPRESS


27. J. Reichardt, U. Wandinger, V. Klein, I. Mattis, B. Hilber, and R. Begbie, "RAMSES: German Meteorological Service autonomous Raman lidar for water vapor, temperature, aerosol, and cloud measurements," Appl. Opt. **51**(34), 8111–8131 (2012).
28. T. Dinoev, V. Simeonov, Y. Arshinov, S. Bobrovnikov, P. Ristori, B. Calpini, M. Parlange, and H. van den Bergh, "Raman Lidar for Meteorological Observations, RALMO – Part 1: Instrument description," Atmos. Meas. Tech. **6**(5), 1329–1346 (2013).
29. E. Hammann and A. Behrendt, "Parametrization of optimum filter passbands for rotational Raman temperature measurements," Opt. Express **23**(24), 30767–30782 (2015).
30. D. N. Whiteman, R. Kurt, and R. Scott, "Airborne and Ground-Based Measurements Using a High-Performance Raman Lidar," J. Atmos. Ocean. Technol. **27**(11), 1781–1801 (2010).
31. B. Liu, Z. Wang, Y. Cai, P. Wechsler, W. Kuestner, M. Burkhart, and W. Welch, "Compact airborne Raman lidar for profiling aerosol, water vapor and clouds," Opt. Express **22**(17), 20613–20621 (2014).
32. D. Wu, Z. Wang, P. Wechsler, N. Mahon, M. Deng, B. Glover, M. Burkhart, W. Kuestner, and B. Heesen, "Airborne compact rotational Raman lidar for temperature measurement," Opt. Express **24**(18), A1210–A1223 (2016).
33. World Meteorological Organisation (WMO), Expert Team, Commission on Basic Systems, Working Group on Satellites, Third session, Final Report, No. 1 (World Meteorological Organization, 1998), p. 73.
34. CEOS, WMO On-line Database, Version 2.5, Observational requirements, http://altostratus.wmo.ch/sat/stations/_asp_htx_idc/Requirements.asp (World Meteorological Organization, 2003).
35. GCOS 2016 Implementation Plan, WMO GCOS-200 (GOOS-214), *https://ane4bf-datap1.s3-eu-west-1.amazonaws.com/wmocms/s3fs-public/programme/brochure/GCOS-200_OnlineVersion.pdf?PlowENiCc1RGh9ReoeAoGBT0QhnJYm6_* (World Meteorological Organization, 2016)
36. D. N. Whiteman, S. H. Melfi, and R. A. Ferrare, "Raman lidar system for the measurement of water vapor and aerosols in the Earth's atmosphere," Appl. Opt. **31**(16), 3068–3082 (1992).
37. D. N. Whiteman, "Examination of the traditional Raman lidar technique. I. Evaluating the temperature-dependent lidar equations," Appl. Opt. **42**(15), 2571–2592 (2003).
38. P. Di Girolamo, M. Cacciani, D. Summa, A. Scoccione, B. De Rosa, A. Behrendt, and V. Wulfmeyer, "Characterization of Boundary Layer Turbulent Processes by the Raman Lidar BASIL in the frame of HD(CP)$^2$) Observational Prototype Experiment," Atmos. Chem. Phys. **17**(1), 745–767 (2017).
39. A. Behrendt, "Temperature measurements with lidar," in *Lidar: Range-Resolved Optical Remote Sensing of the Atmosphere*, Vol. **102** of Springer Series in Optical Sciences, C. Weitkamp, ed. (Springer, 2005), pp. 273–305.
40. E. Hammann, A. Behrendt, F. Le Mounier, and V. Wulfmeyer, "Temperature profiling of the atmospheric boundary layer with rotational Raman lidar during the HDCP2 Observational Prototype Experiment," Atmos. Chem. Phys. **15**(5), 2867–2881 (2015).
41. A. Ansmann, U. Wandinger, M. Riebesell, C. Weitkamp, and W. Michaelis, "Independent measurement of extinction and backscatter profiles in cirrus clouds by using a combined Raman elastic-backscatter lidar," Appl. Opt. **31**(33), 7113–7131 (1992).
42. A. Ansmann, M. Riebesell, and C. Weitkamp, "Measurement of atmospheric aerosol extinction profiles with a Raman lidar," Opt. Lett. **15**(13), 746–748 (1990).
43. R. K. Newsom, D. D. Turner, B. Mielke, M. Clayton, R. Ferrare, and C. Sivaraman, "The use of Simultaneous analog and photon counting detection for Raman lidar," Appl. Opt. **48**(20), 3903–3914 (2009).
44. R. J. List, ed., *Smithsonian Meteorological Tables*, 6th ed. (Smithsonian Institution, 1951), p. 527.
45. World Meteorological Organization, Guide to Meteorological Instruments and Methods of Observation, Appendix 4B, WMO-No. 8, CIMO Guide, (World Meteorological Organization, 2008) Geneva.
46. D. M. Murphy and T. Koop, "Review of the vapour pressures of ice and supercooled water for atmospheric applications," Quart. J. Royal Met. Soc. **131**(608), 1539–1565 (2005).
47. W. P. Elliott and D. J. Gaffen, "Effects of conversion algorithms on reported upper air dewpoint depressions," Bull. Am. Meteorol. Soc. **74**(7), 1323–1325 (1993).
48. D. J. Carson, "The development of a dry inversion-capped convectively unstable boundary layer," Q. J. R. Meteorol. Soc. **99**(421), 450–467 (1973).
49. ESA, "ARMA Reference Model of the Atmosphere," in *Technical Report APP-FP/99–11239/AC/ac* (European Space Agency, 1999).
50. D. M. Winker, J. L. Tackett, B. J. Getzewich, Z. Liu, M. A. Vaughan, and R. R. Rogers, "The global 3-D distribution of tropospheric aerosols as characterized by CALIOP," Atmos. Chem. Phys. **13**(6), 3345–3361 (2013).
51. S. A. Young and M. A. Vaughan, "The retrieval of profiles of particulate extinction from Cloud Aerosol Lidar Infrared Pathfinder Satellite Observations (CALIPSO) data: Algorithm description," J. Atmos. Ocean. Technol. **26**(6), 1105–1119 (2009).
52. X. Lu, Y. Hu, Z. Liu, S. Rodier, M. Vaughan, P. Lucker, C. Trepte, and J. Pelon, "Observations of Arctic snow and sea ice cover from CALIOP lidar measurements," Remote Sens. Environ. **194**, 248–263 (2017).
53. A. J. Illingworth, H. W. Barker, A. Beljaars, M. Ceccaldi, H. Chepfer, N. Clerbaux, J. Cole, J. Delanoë, C. Domenech, D. P. Donovan, S. Fukuda, M. Hirakata, R. J. Hogan, A. Huenerbein, P. Kollias, T. Kubota, T. Nakajima, T. Y. Nakajima, T. Nishizawa, Y. Ohno, H. Okamoto, R. Oki, K. Sato, M. Satoh, M. W. Shephard, A. Velázquez-Blázquez, U. Wandinger, T. Wehr, and G. van Zadelhoff, "The EarthCARE Satellite: The Next

Optics EXPRESS

Step Forward in Global Measurements of Clouds, Aerosols, Precipitation, and Radiation," Bull. Am. Meteorol. Soc. **96**(8), 1311–1332 (2015).
54. K. Gazeas, G. Tzeremes, and E. Armandillo, "Optical study of the laser beam propagation on Nd:YAG crystal slab for space LIDAR missions," Rev. Boliv. Fís. **20s**, 36–38 (2011).
55. G. Ehret, H. H. Klingenberg, U. Hefter, A. Assion, A. Fix, G. Proberaj, S. Berger, S. Geiger, and Q. Lü, "High peak and average power all solid-state laser systems for airborne LIDAR applications," Laser. Opto. **32**, 29–37 (2000).
56. G. Wagner, V. Wulfmeyer, and A. Behrendt, "Detailed performance modeling of a pulsed high-power single-frequency Ti:Sapphire laser," Appl. Opt. **50**(31), 5921–5937 (2011).
57. M. Ostermeyer, P. Kappe, R. Menzel, and V. Wulfmeyer, "Frequency stabilized, diode pumped Nd:YAG laser with up to 0.5 J pulse energy and average output powers of 100W," in *Proceedings of the 22nd International Laser Radar Conference*, ESA SP-561 (European Space Agency, 2004), **Vol. 1**, pp. 57–60.
58. M. Ostermeyer, P. Kappe, R. Menzel, and V. Wulfmeyer, "Diode-pumped Nd:YAG master oscillator power amplifier with high pulse energy, excellent beam quality, and frequency-stabilized master oscillator as a basis for a next-generation lidar system," Appl. Opt. **44**(4), 582–590 (2005).
59. V. Wulfmeyer and J. Bösenberg, "Single-mode operation of an injection-seeded alexandrite ring laser for application in water-vapor and temperature differential absorption lidar," Opt. Lett. **21**(15), 1150–1152 (1996).
60. A. Teppitaksak, A. Minassian, G. M. Thomas, and M. J. Damzen, "High efficiency >26 W diode end-pumped Alexandrite laser," Opt. Express **22**(13), 16386–16392 (2014).
61. S. Ghanbari and A. Major, "High power continuous-wave Alexandrite laser with green pump," Laser Phys. **26**(7), 075001 (2016).
62. S. Ghanbari and A. Major, "High power continuous-wave dual-wavelength alexandrite laser," Laser Phys. Lett. **14**(10), 105001 (2017).
63. C. F. Lillie, "Large Deployable Telescopes for Future Space Observatories," Proc. SPIE **5899**, UV/Optical/IR Space Telescopes: Innovative Technologies and Concepts II, 58990D (International Society for Optical Engineering, 2005).
64. F. Simonetti, A. Zuccaro Marchi, L. Gambicorti, V. Bratina, and P. Mazzinghi, "Large aperture telescope for advanced lidar system," Opt. Eng. **49**(7), 073001 (2010).
65. A. Zuccaro Marchi, F. D'Amato, D. Gallieni, R. Biasi, M. Molina, F. Duò, N. Ruder, P. Salinari, F. Lisi, A. Riccardi, L. Gambicori, F. Simonetti, and J. P. N. Pereira do Carmo, "Technological Developments for Ultra-lightweight, Large aperture, Deployable mirror for space telescopes", presented at the International Conference on Space Optics 2010, Rhodes, Greece, 4 - 8 October 2010.
66. H. Hemmati, Y. Chen, and I. Crossfield, "Telescope Wavefront Aberration Compensation with a Deformable Mirror in an Adaptive Optics System," Free-Space Laser Communication Technologies XVIII, edited by G. Stephen Mecherle, Proc. SPIE **6105**, 61050O, 0277–786X/06/$15 (International Society for Optical Engineering, 2006).
67. J. V. Sandusky, D. J. Hoppe, and M. J. Britcliffe, "Deep Space Optical reception Antenna (DSORA)," in *JPL's IND Progress Report* (NASA, 2000) 42–143, 1–11.
68. P. Mazzinghi, V. Bratina, D. Ferruzzi, L. Gambicorti, F. Simonetti, A. Zuccaro Marchi, P. Salinari, F. Lisi, M. Olivier, A. Bursi, and J. Pereira, "An Ultra-lightweight, Large Aperture, Deployable telescope for Advanced Lidar Applications", in *Proceedings of the 6th Internatational Conference on Space Optics*, ESA SP-621 (European Space Agency, 2006).
69. J. P. Gardner, J. C. Mather, M. Clampin, R. Doyon, M. A. Greenhouse, H. B. Hammel, J. B. Hutchings, P. Jakobsen, S. J. Lilly, K. S. Long, J. I. Lunine, M. J. Mc Caughrean, M. Mountain, J. Nella, G. H. Rieke, M. J. Rieke, H.-W. Rix, E. P. Smith, G. Sonneborn, M. Stiavelli, H. S. Stockman, R. A. Windhorst, and G. S. Wright, "The James Webb Space Telescope," Space Sci. Rev. **123**(4), 485–606 (2006).
70. Y. Arshinov and S. Bobrovnikov, "Use of a Fabry-Perot interferometer to isolate pure rotational Raman spectra of diatomic molecules," Appl. Opt. **38**(21), 4635–4638 (1999).
71. D. N. Whiteman, J. R. Potter, R. Tola, I. Veselovskii, M. Cadirola, K. Rush and J. Comer, "Improvements in Raman Lidar Measurements Using New Interference Filter Technology," in *NASA Technical Report, Paper No. ICNMM2006–96123, Paper Id: 20060026169, NASA Technical Reports Server - NTRS* (NASA, *2006*).
72. M. Scobey, P. Egerton, R. Fortenberry, and A. Czajkowski, "Ultra-narrowband Optical Bandpass Filters with Large Format and Improved Temperature Stability," in *Alluxa White Paper Series. http://www.alluxa.com/learning-center* (2013).
73. S. Adam, A. Behrendt, T. Schwitalla, E. Hammann, and V. Wulfmeyer, "First assimilation of temperature lidar data into a numerical weather prediction model: Impact on the simulation of the temperature field, inversion strength, and planetary boundary layer depth," Q. J. R. Meteorol. Soc. **142**, 2882–2896 (2016).
74. J. R. Campbell, S. Lolli, J. R. Lewis, Y. Gu, and E. J. Welton, "Daytime cirrus cloud top-of-the-atmosphere radiative forcing properties at a midlatitude site and their global consequences," J. Appl. Meteorol. Climatol. **55**(8), 1667–1679 (2016).
75. E. J. O'Connor, A. J. Illingworth, and R. J. Hogan, "A technique for autocalibration of cloud lidar," J. Atmos. Ocean. Technol. **21**(5), 777–786 (2004).
76. U. Wandinger, "Multiple-scattering influence on extinction and backscatter-coefficient measurements with Raman and high-spectral-resolution lidars," Appl. Opt. **37**(3), 417–427 (1998).

Optics EXPRESS

77. A. Macke, "Scattering of Light by Irregular Ice Crystals in Three-dimensional Inhomogeneous Cirrus Clouds," in *Proceedings of the Eighth Conference on Atmospheric Radiation* (American Meteorological Society, 1994), pp. 304–306.
78. J. Kar, M. A. Vaughan, K.-P. Lee, J. L. Tackett, M. A. Avery, A. Garnier, B. J. Getzewich, W. H. Hunt, D. Josset, Z. Liu, P. L. Lucker, B. Magill, A. H. Omar, J. Pelon, R. R. Rogers, T. D. Toth, C. R. Trepte, J.-P. Vernier, D. M. Winker, and S. A. Young, "CALIPSO Lidar Calibration at 532 nm: Version 4 Nighttime Algorithm", Atmos. Meas. Tech. Discuss., https://doi.org/10.5194/amt-2017-365 (2017).
79. W. H. Hunt, D. M. Winker, M. A. Vaughan, K. A. Powell, P. L. Lucker, and C. Weimer, "CALIPSO Lidar description and performance assessment," J. Atmos. Ocean. Technol. **26**(7), 1214–1228 (2009).
80. C. Seckar, L. Guy, A. Di Fronzo, and C. Weimer, "Performance Testing of an Active Boresight Mechanism for Use in the CALIPSO Spaceborne Lidar Mission". Optomechanics, A. E. Hatheway, Ed., Proc. SPIE **5877**, 319–330 (International Society for Optical Engineering, 2005).
81. H. Vömel, D. E. David, and K. Smith, "Accuracy of tropospheric and stratospheric water vapor measurements by the cryogenic frost point hygrometer: Instrumental details and observations," J. Geophys. Res. **112**, D08305 (2007).
82. H. Vömel, M. Fujiwara, M. Shiotani, F. Hasebe, S. J. Oltmans, and J. E. Barnes, "The behavior of the Snow White chilled-mirror hygrometer in extremely dry conditions," J. Atmos. Ocean. Technol. **20**(11), 1560–1567 (2003).
83. GCOS (Global Climate Observing System) Reference Upper-Air Network, (GRUAN), *http://www.wmo.int/pages/prog/gcos/index.php?name=GRUAN*.
84. F. Späth, A. Behrendt, S. K. Muppa, S. Metzendorf, A. Riede, and V. Wulfmeyer, "3-D water vapor field in the atmospheric boundary layer observed with scanning differential absorption lidar," Atmos. Meas. Tech. **9**(4), 1701–1720 (2016).
85. D. D. Venable, D. N. Whiteman, M. N. Calhoun, A. O. Dirisu, R. M. Connell, and E. Landulfo, "Lamp mapping technique for independent determination of the water vapor mixing ratio calibration factor for a Raman lidar system," Appl. Opt. **50**(23), 4622–4632 (2011).
86. V. Simeonov, "First-Principles Calibrated Water Vapor Raman Lidar for Atmospheric Humidity Profiling," presented at the Eighth Symposium on Lidar Atmospheric Applications, 97th AMS Annual Meeting, 22–26 January 2017, Seattle, WA, USA.
87. É. Gérard, D. G. H. Tan, L. Garand, V. Wulfmeyer, G. Ehret, and P. Di Girolamo, "Major advances foreseen in humidity profiling from the Water Vapour Lidar Experiment in Space (WALES)," Bull. Am. Meteorol. Soc. **85**(2), 237–252 (2004).
88. V. Wulfmeyer, H. Bauer, P. Di Girolamo, and C. Serio, "Comparison of active and passive water vapour remote sensing from space: An analysis based on the simulated performance of IASI and space borne differential absorption Lidar," Remote Sens. Environ. **95**(2), 211–230 (2005).
89. European Space Agency, *ADM-Aeolus Science Report - SP-1311*, ISBN 978–92–9221–404–3, ISSN 0379–6566 (European Space Agency, 2008).
90. O. Reitebuch, C. Lemmerz, E. Nagel, U. Paffrath, Y. Durand, M. Endemann, F. Fabre, and M. Chaloupy, "The Airborne Demonstrator for the Direct-Detection Doppler Wind Lidar ALADIN on ADM-Aeolus. Part I: Instrument Design and Comparison to Satellite Instrument," J. Atmos. Ocean. Technol. **26**(12), 2501–2515 (2009).
91. I. Bekey, "An extremely large yet ultra-light weight space telescope and array," (NASA Institute for Advanced Concepts), *http://www.niac.usra.edu/studies/* (1999).
92. N. J. Woolf, "Very large optics for the study of extrasolar terrestrial planets," (NASA Institute for Advanced Concepts), *http://www.niac.usra.edu/studies/*(1999).
93. A. L. Palisoc, "Large telescope using a holographically corrected membrane mirror," (NASA Institute for Advanced Concepts), *http://www.niac.usra.edu/studies/* (2000).

## 1. Introduction

An appropriate understanding and prediction of temperature and water vapour fields is fundamental for a sustainable development of the Earth system. However, our understanding of the water and energy cycles still shows critical gaps on all temporal and spatial scales [1–3]. This is mainly due to a lack of accurate high vertical resolution measurements of water vapour and temperature profiles - hereafter called thermodynamic (TD) profiles - with high temporal-spatial resolution, especially in the lower troposphere [4]. Accurate, high temporal and spatial resolution observations of TD profiles in the lower troposphere from the surface to the interfacial layer at the top of the convective atmospheric boundary layer are essential for improving weather forecasting [e.g., 5, 6] and re-analyses [7]. Furthermore, these measurements are of primary importance to study land-atmosphere (L-A) feedback and to improve parameterizations of land-surface and turbulent transport processes in the ABL, which are essential for regional climate projections [8, 9].

Optics EXPRESS

More specifically, Wulfmeyer *et al.* (2015) [10] demonstrated that global scale measurements of 3-dimensional TD profiles would have a revolutionary impact on our Earth system understanding in four key research areas: i) radiative transfer, as well as the resulting implications on regional and global water and energy budgets, ii) land surface-atmosphere feedback mechanisms including the surface energy balance closure, depending on soil properties and land cover, iii) mesoscale circulations and convection initiation, and (iv) convective-scale data assimilation. Progress in these areas would not only make unique contributions to weather and climate research and forecasting, but also to other related disciplines such as soil, hydrological, and agricultural sciences. These measurements would strongly contribute to better weather forecasting, including the prediction of extreme events, and improvements of climate simulations [3].

However, there is a huge gap in our observational capabilities, particularly from the surface to the lower troposphere. Due to the intrinsic limitations in the inversion of the radiative transfer equation, passive remote sensing systems in space do not provide the quality data required to progress in the above areas, primarily because of their lack in vertical resolution (>1km), insufficient to retrieve vertical gradients in water vapour and temperature profiles, PBL inversions, entrainment processes, etc., particularly for the lower troposphere over land, where surface effects are confounding and IR sounding approaches are limited. Recent results have been achieved in both humidity and temperature profiling by other satellite based techniques like Global Navigation Satellite System - Radio Occultation (GNSS-RO). The GNSS-RO technique provides a combination of global coverage, high vertical resolution (~200 m), high accuracy, and all-weather measurement capability [11]. Precision (random uncertainty) and bias in the middle and upper troposphere for humidity measurements are 10-20% and 5-10%, respectively, while for temperature measurements are 0.5 and 0.2 K, respectively, these values significantly degrading in the lower troposphere [10]. The impact of GNSS-RO measurements of temperature and humidity on both the ECMWF NWP [12, 13] and climate reanalysis [14] systems has been demonstrated to be quite significant, especially for temperature profiling in the UT/LS region and above. Moreover, benefits from GNSS-RO humidity measurements have been reported, especially for tropospheric profiling in cloudy conditions [15]. However, in the lower troposphere, the water vapour and temperature information in the refractivity measurements cannot be disentangled without other information from remote sensing or model output. Furthermore, the measurements can hardly reach below the PBL top due to multipath problems. Therefore, GNSS occultation is likely not suitable for TD profiling in the lower troposphere. Another major limitation of the GNSS-RO technique is represented by its poor horizontal resolution (~450 km), as in fact around 70% of the bending occurs over a 450 km section of ray-path.

These observational gaps can be closed by the development and operation of an active remote sensing system in space based on the Raman lidar technique [16]. By a combined detection of vibrational and rotational Raman signals using a single laser transmitter, simultaneous and independent measurements of water vapour and temperature profiles and a variety of derived variables are possible. These can be performed with unprecedented vertical resolution of 100-200 m and horizontal resolution down to 20 km, especially in the lower troposphere. In this region Raman lidar measurements close a gap in accurate water vapour and temperature profiling. This unique information content will also complement GNSS-RO measurements, which encourages a synergetic application of the two techniques.

An instrumental concept for a space Raman lidar is proposed in this paper and the specifications of the different sub-systems are defined and verified through the application of a performance simulation model [16]. Methodological approaches and technological solutions proposed in the paper refer to the long-term research experience matured in the scientific community in developing and operating ground-based [17–29] and airborne instruments [30–32]. The performance of the proposed space-borne water vapour and temperature Raman lidar has been simulated under a variety of environmental and climate conditions. For this purpose, different atmospheric reference models, covering various

Optics EXPRESS

climatic regions and seasons, as well as a variety of solar illumination conditions, were considered. Reported simulations cover both clear-sky and cloudy conditions.

These simulations represent the baseline for future proposals for an atmospheric thermodynamics space-borne Raman lidar to International Space Agencies. A successful implementation of the proposed mission concept will likely require the combined support of two or more International Space Agencies, joining their forces in terms of technological skills and budgetary resources.

Observational requirements to be fulfilled by networks of satellite and ground-based remote sensors, with a specific focus on lower troposphere, have been identified by Wulfmeyer *et al.* (2015) [10], considering four primary application fields: (1) monitoring, (2) verification and calibration, (3) data assimilation (DA), and (4) process studies (https://www.wmo-sat.info/oscar/observingrequirements). These requirements, which are found to be similar for the various applications, imply the use of a vertical resolution in the range 10–100 m, i.e. sufficiently high to allow resolving temperature and moisture gradients in the lower troposphere. Measurements are required at the mesoscale, with high horizontal resolution and a specific covering capability from the meso-beta (20–200 km) to the meso-gamma (2–20 km) scales. In each single vertical range bin the bias affecting water vapour mixing ratio and temperature measurements should be in the range 2–5% and 0.2–0.5 K, respectively, while the random uncertainty should be smaller than 10% and 1 K, respectively. These observational requirements also include those defined by World Meteorological Organization [33, 34] and the World Climate Research Program (WCRP). More recently, the World Meteorological Organization has refined recommendations for a functional and robust Global Climate Observing System (GCOS), identifying more stringent observational requirements for both temperature and humidity profiling [35], especially with respect to the requirements in terms of measurement stability (GCOS/ESA-CCI 0.3% per decade) needed for the detection of climate signals/trends. Simulations reported in this paper confirm that observational requirements for most numerical weather prediction and climate research applications can be fulfilled in the low-mid troposphere by a Raman lidar system deployed on-board a low-Earth-orbit satellite in clear sky conditions, as well as above clouds, through broken clouds and through/below overcast thin clouds, under a variety of climatic scenarios and seasons. A space mission hosting a payload as the one described in this paper would collect a very ample and comprehensive data set for the monitoring of the Earth's weather and climate system.

The outline of the paper is the following. In Section 2 the Raman lidar techniques are illustrated, with a specific focus on atmospheric water vapour mixing ratio and temperature measurements. Section 3 provides a detail description of the analytical model used in the simulations and illustrates the procedure used to assess measurement precision; section 4 describes the instrumental concept at the basis of the simulations, briefly illustrating the considered technological solutions and providing specifications of all major sub-systems of the lidar. The main results of the simulations are outlined and discussed in section 5. Finally, section 6 summarizes all results and provides some indications for possible future work.

## 2. Raman lidar techniques

Based on the application of the vibrational Raman lidar technique, the vertical profile of atmospheric water vapour mixing ratio, $x_{H_2O}(z)$, can be obtained from the power ratio of water vapour to molecular nitrogen vibrational Raman signals through the application of the analytical expression [36]:

$$x_{H_2O}(z) = K(z) \cdot \frac{P_{H_2O}(z)}{P_{N_2}(z)} \tag{1}$$

where $P_{H_2O}(z)$ and $P_{N_2}(z)$ are the water vapour and molecular nitrogen vibrational Raman lidar signals at $\lambda_{H_2O}$ and $\lambda_{N_2}$, respectively, expressed in terms of photon numbers, received from the scattering volume at altitude *z* (range in case of an off-nadir pointing system), and $K(z) = k \cdot f_1(z) \cdot f_2(z)$ is a calibration function obtained by multiplying two height-dependent correction terms ( $f_1(z)$ and $f_2(z)$ ) and a height-independent calibration factor, *k* (e.g [36–38]. In expression (1) the signal $P_{N_2}(z)$ is used as a reference signal for the determination of the water vapour mixing ratio, as in fact molecular nitrogen is a well-mixed species, with a constant mixing ratio, throughout the homosphere (up to approx. 100 km).

$f_1(z)$ is the differential transmission term accounting for the different atmospheric transmission by molecules and aerosols at $\lambda_{H_2O}$ and $\lambda_{N_2}$, while $f_2(z)$ is a temperature-dependent term associated with the use of a narrowband interference filter for the spectral selection of $P_{H_2O}(z)$. The height-independent calibration factor *k* is obtained by comparing the quantity $f_1(z) \cdot f_2(z) \cdot \left[ P_{H_2O}(z) / P_{N_2}(z) \right]$ with simultaneous and co-located mixing ratio measurements from a different sensor (e.g., from radiosondes, microwave radiometers, GNSS integrated water vapour). Uncertainties in the determination of the calibration function *K(z)* may lead to a residual systematic uncertainty (bias) affecting water vapour measurements, typically not exceeding ± 3-5%.

Based on the application of the pure rotational Raman lidar technique, the vertical profile of atmospheric temperature, *T(z)*, is obtained from the power ratio of high-to-low quantum number rotational Raman signals, *Q*(*T*), through the inversion of the analytical expression:

$$Q(z) = P_{HiJ}(z) / P_{LoJ}(z) = \exp\left[\alpha / T(z) + \beta\right] \tag{2}$$

where $P_{LoJ}$(z) and $P_{HiJ}$(z) are the low (*LoJ*) and high (*HiJ*) quantum number rotational Raman signals at $\lambda_{LoJ}$ and $\lambda_{HiJ}$, respectively, expressed in terms of photon numbers, received from the scattering volume at altitude *z* in the anti-Stokes branch, and $\alpha$ and $\beta$ are two calibration constants. Thus, *T(z)* can be obtained through the expression:

$$T(z) = \frac{\alpha}{\ln[Q(z)] - \beta} \tag{3}$$

where $\alpha$ and $\beta$ are determined by comparing the lidar signals' power ratio *Q(z)* with simultaneous and co-located temperature measurements from a different sensor (again, radiosondes or microwave radiometers). Uncertainties in the determination of the two calibration constants may lead to an overall residual systematic uncertainty (bias) on temperature measurements, typically not exceeding ± 0.3-0.5 K [16]. Besides expression (3), alternative more complex analytical expressions relating *Q*(*T*) to *T(z)* can be defined [39], i.e. considering a second- or third-order polynomial functions and three or four calibration constants, with the overall systematic uncertainty affecting temperature measurements being comparably small (0.1-0.2 K [23]).

The water vapour vibrational Raman lidar signal $P_{H_2O}(z)$, expressed as number of collected photons, can be written as:

$$P_{H_2O}(z) = \frac{\lambda_0 E_0}{hc} \frac{A_{tel}}{z^2} \eta \frac{c\tau}{2} n_{H_2O}(z) \sigma_{H_2O} T_{\lambda_0}(z) T_{\lambda_{H_2O}}(z) + bk_{H_2O} \tag{4}$$

where $E_0$ is the laser pulse energy at the laser wavelength $\lambda_0$, *c* is the speed of light in air, *h* is the Planck's constant, $A_{tel}$ is the telescope area, $\eta$ is the overall transmitter–receiver efficiency

(including, among others, the laser transmission optics reflectivity, the telescope primary-secondary mirror reflectivity, the interference filter transmission efficiency and the detector quantum efficiency) at wavelength $\lambda_{H_2O}$, $\tau$ is the laser pulse duration, $n_{H_2O}(z)$ represents the water vapour number density at altitude *z*, $\sigma_{H_2O}$ is the water vapour roto-vibrational Raman cross-section, $T_{\lambda_0}(z)$ and $T_{\lambda_{H_2O}}(z)$ are the atmospheric transmission profiles from the satellite down to the scattering volume at altitude *z* at $\lambda_0$ and $\lambda_{H_2O}$, respectively, and the term $bk_{H_2O}$ represents the background signal collected by the telescope and detected by the water vapour Raman channel.

In expression (1) the reference signal $P_{N_2}(z)$ can be replaced by an alternative temperature-independent reference signal, $P_{ref}(z)$, obtained as a linear combination of the two temperature sensitive rotational Raman lidar signals $P_{LoJ}(z)$ and $P_{HiJ}(z)$, based on the weighted sum [20]:

$$P_{ref}(z) = P_{LoJ}(z) + cP_{HiJ}(z) \tag{5}$$

This alternative approach is considered in the system concept illustrated in this paper. The weighting term *c* depends on the system characteristics [20, 40] and is determined by calculating the temperature dependence of each rotational Raman (RR) signal, taking the spectral characteristics of the receiver into account, and then determining a combination of the RR signals with minimum temperature variation, with the residual temperature sensitivity being typically smaller than 0.2% in the interval 180–270 K [16]. When stimulated with laser radiation at $\lambda_0$ = 354.7 nm, i.e. the ultraviolet (UV) wavelength emitted by a frequency-tripled Nd:YAG laser source), $P_{H_2O}(z)$ is collected at $\lambda_{H_2O}$ = 407.5 nm, while $P_{LoJ}(z)$ and $P_{HiJ}(z)$ are collected at $\lambda_{LoJ}$ = 354.36 nm and $\lambda_{HiJ}$ = 353.29 nm, respectively. As $P_{ref}(z)$ is a weighted summation of $P_{LoJ}(z)$ and $P_{HiJ}(z)$, its wavelength $\lambda_{ref}$ is tentatively assumed to be located at $(\lambda_{LoJ} + \lambda_{HiJ})/2$, i.e. 353.8 nm.

The pure rotational Raman lidar signals $P_{LoJ}(z)$ and $P_{HiJ}(z)$, can be expressed as:

$$P_{LoJ/HiJ}(z) = \frac{\lambda_0 E_0}{hc}\frac{A_{tel}}{z^2}\eta\frac{c\tau}{2}\sum_{i=N_2,O_2}\sum_{Ji=1}^{n}\left[n_i(z)\tau_{RR}(J_i)F_{J_i}(T)\frac{d\sigma_{J_i}}{d\Omega}\right]\times \\ \times T_{\lambda_0}(z)T_{\lambda_{LoJ/HiJ}}(z) + bk_{LoJ/HiJ} \tag{6}$$

where $E_0$, $\lambda_0$, *c*, *h*, $A_{tel}$, $\eta$ *and* $\tau$ have already been defined above, while $n_i(z)$ represents the number density of $N_2$ and $O_2$, $\tau_{RR}(J_i)$ is the interference filter spectral profile at the wavelength corresponding to the rotational Raman line with quantum number $J_i$, $F_{J_i}(T)$ is the normalized distribution for the $N_2/O_2$ excited rotational levels at temperature *T*, $\frac{d\sigma_{J_i}}{d\Omega}$ is the differential rotational Raman backscatter cross section of the $N_2$ and $O_2$ transition from the initial energy level with rotational quantum number $J_i$ to the energy level with $J_i \pm 2$. Additionally, in expression (6), $T_{\lambda_0}(z)$ and $T_{\lambda_{LoJ/HiJ}}(z)$ are the atmospheric transmission profiles from the satellite down to the scattering volume at altitude *z* at the laser wavelength $\lambda_0$ and at the centre wavelength of the low-*J* ($\lambda_{LoJ}$) and high-*J* ($\lambda_{HiJ}$) rotational Raman bands, respectively, and the term $bk_{LoJ/hiJ}$ represents the background signals collected by the telescope and detected by the low- and high-*J* rotational Raman channels.

The location of $\lambda_{LoJ}$ and $\lambda_{HiJ}$ can be identified based on a sensitivity analysis accounting for a variety of atmospheric and instrumental parameters as the signal-to-background ratio,

the temperature range of interest, the filter bandwidth and filter shape, etc. Hammann and Behrendt (2015) [29] defined a simple parameterization approach to identify the optimal location of $\lambda_{LoJ}$ and $\lambda_{HiJ}$. In the present study $\lambda_{LoJ}$ and $\lambda_{HiJ}$ were identified with the purpose of optimizing daytime measurement performances in the Convective Planetary Boundary Layer. For this purpose, the approach by Hammann and Behrendt (2015) [29] suggests the selection of the portions of low- and high-quantum number rotational anti-Stokes branch shifted by 26.78 and 111.94 $cm^{-1}$, respectively, with respect to the laser wavelength. When considering a laser emission at $\lambda_0$ = 354.7 nm, $\lambda_{LoJ}$ and $\lambda_{HiJ}$ are located at 354.36 and 353.29 nm, respectively.

The vertical profile of the particle backscattering coefficient, $\beta_{\lambda_0}^{par}(z)$, can be obtained from the power ratio of the elastic backscatter signal $P_{\lambda_0}(z)$ to the temperature-independent reference signal $P_{ref}(z)$, defined in expression (5), through a modified form of the analytical expression defined by Ansmann *et al.* (1992) [41]:

$$\beta_{\lambda_0}^{par}(z) = \beta_{\lambda_0}^{mol}\left[\frac{P_{\lambda_0}(z)}{k \cdot P_{ref}(z)} - 1\right] \tag{7}$$

where $\beta_{\lambda_0}^{mol}(z)$ represents the molecular contribution to the backscattering coefficient, associated with Rayleigh scattering from ambient air molecules, and $k$ is a normalization term. $\beta_{\lambda_0}^{mol}(z)$ is obtained from a dry air number density profile $n(z)$, which in turn is determined from available atmospheric temperature and pressure profiles (for example, from sensors as radiosondes or microwave radiometers, or from an atmospheric model). $k$ is determined by normalizing the elastic backscatter signal $P_{\lambda_0}(z)$ to the reference signal $P_{ref}(z)$ at a reference height $z_0$, usually above the Planetary Boundary Layer (PBL) and outside clouds or aerosol layers, selected in a way to satisfy the condition $\beta_{\lambda_0}^{mol}(z) >> \beta_{\lambda_0}^{par}(z)$. Expression (7) differs from the one proposed by Ansmann *et al.* (1992) [41] as in fact, because of the consideration of a reference signal at a wavelength ($\lambda_{ref}$ = 353.8 nm) very close to the laser wavelength $\lambda_0$, the differential transmission term originally included in this expression can be assumed to be equal to 1. In fact, the deviation of the differential transmission term from 1 is less than 1% from surface up to an altitude of 10 km and less than 1.4% from surface up to an altitude of 30 km and, consequently, the systematic effect associated with this assumption is far smaller than the random uncertainty affecting the particle backscattering coefficient measurement. The elastic backscatter signal $P_{\lambda_0}(z)$ can be expressed as:

$$P_{\lambda_0}(z) = \frac{\lambda_0 E_0}{hc}\frac{A_{tel}}{z^2}\eta\frac{c\tau}{2}\left[\beta_{\lambda_0}^{mol}(z) + \beta_{\lambda_0}^{par}(z)\right]T_{\lambda_0}^2(z) + bk_{\lambda_0} \tag{8}$$

where $T_{\lambda_0}(z)$ is the atmospheric transmission profiles from the satellite down to the scattering volume at altitude $z$ at $\lambda_0$ and the term $bk_{\lambda_0}$ represents the background signal collected by the telescope and detected by the elastic backscatter channel.

The vertical profile of the particle extinction coefficient, $\alpha_{\lambda_0}^{par}(z)$, at $\lambda_0$ = 354.7 nm can be obtained from $P_{ref}(z)$ through the application of a modified form [16] of the equation defined by Ansmann *et al.*(1990) [42]:

Optics EXPRESS

$$\alpha_{\lambda_0}^{par}(z) = \frac{1}{2}\frac{d}{dz}\ln\left\{\frac{n(z)}{P_{ref}(z)\cdot z^2}\right\} - \alpha_{\lambda_0}^{mol}(z) \quad (9)$$

where $\alpha_{\lambda_0}^{mol}(z)$ is the extinction coefficient at 354.7 nm associated with Rayleigh scattering by atmospheric molecular species and *n(z)* represents the ambient gas number density; both these terms are determined from available atmospheric temperature and pressure profiles, e.g. from co-located radiosonde data or a model atmosphere. Again, expression (9) differs from the one proposed by Ansmann *et al.* (1990) [42] as, because of the vicinity of the laser and reference signal wavelengths, the extinction coefficient at these two wavelengths can be assumed identical.

## 3. Model

A lidar simulator, developed at Scuola di Ingegneria (formerly Dipartimento di Ingegneria e Fisica dell'Ambiente), Università degli Studi della Basilicata [16], has been applied in this paper to assess the expected performances of a space-borne water vapour and temperature Raman lidar system, exploiting the vibrational and pure rotational Raman techniques in the UV. This analytical simulator allows assessing measurement quality in terms of both systematic and random measurement uncertainties. The specifications of the different lidar sub-systems have been defined and/or verified based on the application of this performance model. The performance of the present simulator has been verified against ground-based Raman lidars for water vapour mixing ratio and temperature measurements [10] and against the space-borne lidar CALIOP for particle backscatter measurements.

Simulations consider a sun-synchronous low Earth orbit, with an orbiting height and speed of 450 km and 7 km/s, respectively. A dawn-dusk orbit with an ascending node crossing time of 6 h (i.e. with overpasses at 6/18 h local time) has been selected for the simulations. This orbit selection allows capturing the thermodynamic state before and after the daytime development of the PBL, which is beneficial for data assimilation in weather forecast models [10].

The statistical uncertainties affecting water vapour mixing ratio, temperature and particle backscattering and extinction coefficient measurements are determined through error propagation from the statistical (or random) uncertainties affecting elastic and Raman backscatter lidar signals, these latter being estimated based on the application of Poisson statistics to signal photon counts. In this regard, it is to be pointed out that the application of Poisson statistics to lidar signals is well-suited in case of data acquired in photon-counting or analogical mode, in the latter case after conversion of the analogical signals into "virtual" counts [43].

Specifically, the percentage random uncertainty affecting water vapour mixing ratio measurements can be determined through the following analytical expression [37]:

$$\frac{\Delta x_{H_2O}(z)}{x_{H_2O}(z)} = 100\times\sqrt{\frac{P_{H_2O}(z)+bk_{H_2O}}{P_{H_2O}^2(z)} + \frac{P_{ref}(z)+bk_{ref}}{P_{ref}^2(z)}} \quad (10)$$

This expression assumes detectors' noise (dark current) to be negligible with respect to the background noise. A similar expression applies for the random uncertainty affecting temperature measurements [18]:

$$\Delta T(z) = \frac{\partial T(z)}{\partial R}R(z)\sqrt{\frac{P_{loJ}(z)+bk_{loJ}}{P_{loJ}^2(z)} + \frac{P_{hiJ}(z)+bk_{hiJ}}{P_{hiJ}^2(z)}} \quad (11)$$

Here, again, detectors' dark current is assumed to be negligible with respect to the background noise. Most cloud microphysical studies require the measurement of relative

humidity (*RH*). As this quantity is a function of atmospheric temperature and water vapour mixing ratio, the random uncertainty affecting *RH* measurements can be calculated from the random uncertainty affecting these two quantities through the expression:

$$\frac{\Delta RH(z)}{RH(z)} = \sqrt{\left(\frac{\Delta x_{H_2O}(z)}{x_{H_2O}(z)}\right)^2 + \varepsilon\left(\frac{\Delta e_s(z)}{e_s(z)}\right)^2} \tag{12}$$

with $e_s$ being the water vapour saturation pressure and $\varepsilon = M_w/M_d$ being the ratio of water molecular weight, $M_w$ = 18 g/mole, over the dry air apparent molecular weight, $M_d$ = 28.7 g/mole. This expression assumes the uncertainty affecting atmospheric pressure measurements to be negligible with respect to the uncertainties affecting water vapour mixing ratio and temperature measurements. Different formulation of $\Delta e_s(z)/e_s(z)$ can be given in dependence of the considered expression relating the water vapour saturation pressure to atmospheric temperature. A commonly used expression [44], following WMO guidelines [45], is:

$$e_s(z) = c\exp\left\{\frac{a\left[T(z) - 273.15K\right]}{T(z) - 273.15K + b}\right\} \tag{13}$$

with $a$ = 17.08/17.84 and $b$ = 234.2/245.4 K for temperatures above/below the freezing level, while $c$ is equal to 6.107. In this case:

$$\frac{\Delta RH(z)}{RH(z)} = \sqrt{\left(\frac{\Delta x_{H_2O}(z)}{x_{H_2O}(z)}\right)^2 + \varepsilon^2\left\{1 - \frac{abT(z)}{\left[T(z) - 273.15 + b\right]^2}\right\}^2\left(\frac{\Delta T(z)}{T(z)}\right)^2} \tag{14}$$

It is to be pointed out that, while most formula used to estimate the water vapour saturation pressure $e_s$ lead to very close values for temperatures above the freezing level, non-negligible differences may appear below the freezing level, with consequent systematic effects on relative humidity measurements. This potential source of bias may be critical in cirrus cloud studies, where accurate estimates of the degree of ice super-saturation with respect to water are necessary. In this respect, it was quantified that deviations between different formula range from –6% to + 3% at –60°C and from –9% to + 6% at –70°C [46]. For temperature values typically found in the low and mid troposphere, the influence of the saturation vapor pressure formula on RH is small and only significant for climatological studies [47].

The percentage random uncertainty affecting the measurement of $\beta_{\lambda_0}^{par}(z)$ is given by:

$$\frac{\Delta\beta_{\lambda_0}^{par}(z)}{\beta_{\lambda_0}^{par}(z)} = 100\times\sqrt{\left(\frac{\Delta\beta_{\lambda_0}^{mol}}{\beta_{\lambda_0}^{mol}}\right)^2 + \left(\frac{P_{\lambda_0}(z)/k\cdot P_{ref}(z)}{P_{\lambda_0}(z)/k\cdot P_{ref}(z) - 1}\right)^2\cdot\left[\frac{P_{\lambda_0}(z) + bk_{\lambda_0}}{P_{\lambda_0}^2(z)} + \frac{P_{ref}(z) + bk_{ref}}{P_{ref}^2(z)}\right]} \tag{15}$$

while the random uncertainty affecting the measurement of $\alpha_{\lambda_0}^{par}(z)$ is given by [16]:

$$\Delta\alpha_{\lambda_0}^{par}(z) = \frac{1}{\sqrt{2}\Delta z}\frac{\Delta P_{ref}(z)}{P_{ref}(z)} \tag{16}$$

with $\Delta z$ being the vertical resolution of the extinction measurement. Expression (16) can be expressed as a percentage random uncertainty in the form [16]:

Optics EXPRESS

$$\frac{\Delta\alpha_{\lambda_0}^{par}}{\alpha_{\lambda_0}^{par}}(z)=\frac{100}{\sqrt{2}\Delta\tau}\frac{\Delta P_{ref}(z)}{P_{ref}(z)} \tag{17}$$

with $\Delta\tau$ being aerosol optical thickness within the vertical interval $\Delta z$.

It is to be pointed out that percentage random uncertainty is used for water vapour mixing ratio, relative humidity and aerosol optical properties, while absolute random uncertainty is used for temperature. This is because water vapour and aerosol concentrations may show a large space and time variability, larger than the one characterizing atmospheric temperature. This large variability strongly reverberates on the absolute uncertainty, which can consequently largely deviate from the climatological value. The percentage random uncertainty is a good representation of measurement precision. This implies a lower percentage uncertainty affecting the measurement where the observed constituent is more abundant. Because of the slowly decreasing trend with altitude characterizing the temperature profile, the absolute random uncertainty is a better representation of its measurement precision.

Atmospheric quantities considered in the simulation include vertical profiles of pressure, temperature, and humidity from three selected atmospheric reference models (tropical, mid-latitude, this latter with both summer and winter options, and U.S. Standard Atmosphere 1976, Fig. 1 in [10]). The use of atmospheric reference models based on climatological profiles allows to assess system performance in average conditions, but not in extreme conditions. For the purpose of contemplating more extreme conditions, in this study we are also considering the radiosonde profiles used in the paper by Wulfmeyer *at al.*, 2015 [10, Figs. 9(a-b)], where thermodynamic profiling capabilities from a variety of advanced remote sensors are compared. The considered radiosonde observation occurred at 11:30 UTC on 21 September 2007 during the ARM Mobile Facility deployment in the Black Forest in southwest Germany. The selected radiosonde profiles of temperature and humidity are characterized by the presence of a number of dry lamina and a temperature inversions in the lower troposphere, which are critical features having an important role in inhibiting/triggering convective activity and the development of severe weather events (among others [48]). These radiosonde profiles allow assessing extreme values of the random uncertainty experienced in the presence of strong humidity and temperature gradients and reveal the unprecedented performances of Raman lidars vs. any other active or passive remote sensing technique in the lower troposphere.

Aerosol optical properties are simulated based on the use of the median aerosol extinction data from the ESA Aerosol Reference Model of the Atmosphere (ARMA [49], illustrated in Fig. 5). Besides a boundary layer contribution, extending up to approx. 1.5 km (with values of $\beta_{\lambda_0}^{par}(z)$ in the range 0.4-2.8 × $10^{-6}$ $m^{-1}$ $sr^{-1}$), this model also includes a free- tropospheric aerosol layer, extending from 1.5 km up to 2.5 km (with values of $\beta_{\lambda_0}^{par}(z)$ in the range 0.03-0.4 × $10^{-6}$ $m^{-1}$ $sr^{-1}$), influenced by the underlying surface characteristics, and a mid- and upper-tropospheric aerosol layer, extending from 2.5 km all the way up to the tropopause, with aerosol concentration - and consequently $\beta_{\lambda_0}^{par}(z)$- slowly decreasing with altitude (down to $\beta_{\lambda_0}^{par}(z)$ values of 2 × $10^{-9}$ $m^{-1}$ $sr^{-1}$ at 15 km). The model also includes a stratospheric aerosol layer, with values of $\beta_{\lambda_0}^{par}(z)$ decreasing down to 5 × $10^{-11}$ $m^{-1}$ $sr^{-1}$ around 30 km. The ARMA aerosol model considers different constant values of the extinction-to-backscattering ratio (lidar ratio), LR, in the different aerosol layers. Specifically, a value of LR equal to 40 sr is considered in the boundary layer, while a value of 30 sr is considered above. These LR values are intended to be typical for the boundary layer and the free troposphere, as in fact sensitively different values may be found in these

two regions in the presence of specific aerosol types (e.g. dust in the free troposphere, with LR = 45 sr at 354.7 nm or highly absorbing aerosols, with LR values often exceeding 60 sr). Model values of $\alpha_{\lambda_0}^{par}(z)$ are obtained from the values of $\beta_{\lambda_0}^{par}(z)$ and LR. In the present simulations we are also considering the aerosol backscatter/extinction climatological analysis reported by [50] based on the global 3-D distribution measurements of tropospheric aerosols by the Cloud-Aerosol Lidar with Orthogonal Polarization (CALIOP) on board Cloud-Aerosol Lidar and Infrared Pathfinder Satellite Observations (CALIPSO) since June 2006. Specifically, we considered two 6-yr mean nighttime summer profiles (over Eastern US, 31–41 °N, 95–75 °W, during July 2006–2011, and over South-Eastern Asia, 1–19 °N, 90–110 °E, during August 2006–2011) and two 5-yr mean nighttime winter profiles (over the Arctic profiles, 61–82 °N, January 2007–2011and March 2007–2011). Mean nighttime summer profiles are considered as in fact the aerosol detection thresholds are higher during daytime than at night because of the signal-to-noise reduction by solar background illumination, enabling the detection of weakly scattering layers which may be missed during daytime [50]. Aerosol extinction profiles at 532 nm and 1064 nm in this climatological data set are determined from the lidar backscatter profiles at these same wavelengths using estimated lidar ratios for six specific aerosol types defined in the CALIOP retrieval (Dust, Polluted Dust, Marine, Clean Continental, Pollution, and Biomass Burning [51]), with values in the range 20–70 sr.

An analytical expression for daylight background signals collected by the various lidar channels has been formulated and tested in Di Girolamo *et al*. (2006) [16]. This expression includes three distinct contributions: namely, a cloud-free atmospheric contribution, a surface contribution and a cloud contribution. The cloud-free atmospheric contribution, $bk_{atm}$, accounts for solar radiation scattering by atmospheric constituents (molecular species and aerosols); the surface contribution, $bk_{surf}$, accounts for solar radiation reflection by the Earth surface, while the cloud contribution, $bk_{cloud}$, accounts for the solar radiation reflection by clouds. All three contributions depend on the solar zenith angle. Thus a sun-synchronous low Earth dusk/dawn orbit, because of its low solar zenith angles, is advantageous also in this respect. Furthermore, background signals are proportional to the second power of the receiving telescope field of view (FOV). Consequently, background signals can be reduced by selecting small FOVs, which, however, may increase optical layout complexity. In estimating daylight background signals, a default value for the Earth surface albedo of 0.3 has been considered, which represents the globally-averaged value for this parameter. An analysis has been carried out to estimate the sensitivity of results to the variability in surface albedo in order to identify possible surface typologies leading to improvements or degradations of measurement performances. This sensitivity analysis for water vapour measurements confirmed the same results already reported for atmospheric temperature measurements [16], i.e. measurement precision above strongly absorbing surfaces (sea surface at low Sun angle, albedo = 0.1) is only 3–5% higher than above strongly reflecting surfaces (snow surface at high Sun angle, albedo = 0.95), and thus the dependence of system performances on surface albedo is weak. Estimates of snow/ice surface reflectance have been obtained from CALIOP measurements of surface integrated attenuated backscatter color ratio and integrated depolarization ratio [52], leading to values around 0.8 in the visible, which are compatible with the selected values in our simulations.

## 4. Instrumental concept

In the present mission concept, the Raman lidar is conceived and designed to collect four primary lidar signals: the water vapour vibrational Raman signal, $P_{H_2O}(z)$, the high- and low-quantum number rotational Raman signals, $P_{LoJ}(z)$ and $P_{HiJ}(z)$, and the elastic backscatter signal at $\lambda_0$, $P_{\lambda_0}(z)$, following a layout originally proposed by Behrendt *et al.* (2002) [20]. As specified above, there is no need for the collection of the molecular nitrogen

Optics EXPRESS

vibrational Raman signal; this is because an alternative temperature-insensitive reference signal ($P_{ref}$(z), see expression (5)) is obtained from the combination of the temperature-sensitive rotational Raman signals $P_{LoJ}$(z) and $P_{HiJ}$(z). The use of this alternative reference signal instead of the weaker molecular nitrogen vibrational Raman signal leads to a reduction of the random uncertainty affecting water vapour mixing ratio measurements in the Planetary Boundary Layer up to 4% and 1% for night time and daytime measurements, respectively. The four detected signals allow for independent measurements of atmospheric temperature, water vapour mixing ratio (and consequently relative humidity) and particle backscattering and extinction coefficients at $\lambda_0$ = 354.7 nm [18], these latter two variables such as delivered by the EarthCARE mission [53], albeit with a much more powerful laser source and thus significantly higher temporal and spatial resolutions. Furthermore, very valuable additional products can be independently measured: i.e. the true PBL depth over land and the oceans (derived from the temperature profiles) and the geometric (cloud top height, cloud base height in case optically thin mid-level and cirrus clouds) and optical properties of clouds (cloud optical depth for optically thin clouds, as well as backscatter and extinction profiles within these clouds). The PBL depth measurement is a unique feature of this instrument, as in fact this derivation - based on true temperature profiles - is not possible with any other satellite instrument.

The payload is intended to be hosted on satellite deployed on a sun-synchronous orbit at an altitude of 450 km (inclination ~97 degrees), characterized by an ascending node crossing time of 6 h. A compromise altitude of 450 km is considered as in fact lower altitudes (< 400 km) may lead to a large atmospheric drag of the hosting space platform, which may ultimately require regular altitude boosts. This would consequently lead to a larger fuel consumption and, consequently, a shorter life-time of the mission. On the other hand, a higher orbiting altitude yields degradation of the collected signals. A 3° off-nadir transmission of the laser beam is considered to avoid specular reflections from ice crystals.

In the following sub-sections we illustrate and discuss recent advances achieved in the design and development of solid-state lasers, large-aperture telescopes, and in detector technologies, allowing for reaching a new performance level from space. The system specifications resulting from these technological advances have been incorporated in the performance simulations.

### *4.1 Lidar transmitter*

The lidar transmitter considered in our simulations consists of a frequency-tripled, diode-laser pumped Nd:YAG laser, with an electrical-to-optical efficiency of >10% and an average power in the UV (at 354.7 nm) of at least 250 W (beam quality: $M^2$ < 20). The required UV laser power can be achieved based on the use of a new generation of pump chambers, with efficient pumping by diode lasers [54]. The baseline to achieve the large UV laser power needed for space Raman lidar applications is represented by the inclusion of several (4 to 6) amplification stages, each one embedding high-density stacks of pumping diodes. The exploitation of diode laser pumping determines radiative or conductive cooling to be sufficient, also in case of space implementation. Relying on an overall electric-to-354.7-nm efficiency in excess of 10%, a laser optical power of >250 W at 354.7 nm can be achieved based the electrical power available on most space platforms and provided by on-board solar arrays.

It is to be recalled that, for a given average optical power, better performances are achieved considering high single pulse energies and lower repetition rates than the other way around. In the following simulations we refer to a compromise configuration including a laser source with a repetition rate of 100 Hz and emitting pulses at 354.7 nm, with a single pulse energy of 2.5 J. Besides the number amplification stages, the optical design for the laser source considered in our simulations is very similar to the one implemented in the two-wavelength elastic backscatter lidar CALIOP, whose performance, after more than 10 years of continuous on-orbit operation, has demonstrated to keep high in terms of energy stability.

Optics EXPRESS

The technological feasibility of such laser source refers to the experience recently gained at the University of Hohenheim (UHOH) and other German scientific institutions in the design and development of the high-power Nd:YAG laser transmitters [55–58]. Furthermore, this laser concept is considerably less complex than the ADM-Aeolus and the EarthCARE laser transmitter because it requires a simple frequency stabilization unit, already widely used in commercially available laser sources, and does not require beam shaping optics and specific operation modes with respect to repetition rates and bursts. The development of this laser concept will strongly benefit from the maturity gained in the design, development, and space qualification of laser subsystems in the frame of the ADM-Aeolus and EarthCARE missions, especially for what concerns the space-qualified pump diodes.

Alternative designs and technical solutions for the laser source are also being investigated for the purposes of this study. Specifically, an Alexandrite laser source was considered [59]. The main advantages of a laser source based on this lasing material (chryso-beryl crystal, $BeAl_2O_4$, doped with active chromium ions, $Cr_{3+}$) is represented by the capability to generate pulses with a fundamental emission at wavelengths between 700 and 820 nm, shorter than the one emitted by Nd:YAG lasers, so that suitable UV wavelengths can be obtained by simply doubling instead of tripling the lasing frequency. In-band pumping at 650 nm will also increase the efficiency of operation by decreasing the quantum defect. This has important implications in terms of the achievable electric-to-optical conversion efficiency, as second-harmonic generators' conversion efficiencies are usually 2-3 times larger than those of third-harmonic generators. An additional important advantage of Alexandrite laser sources is the increase of gain with increasing temperature of the lasing material. This aspect makes the exploitation of this lasing material particularly interesting for space implementation as in fact, as a result of the improved laser performance at elevated temperatures, laser cooling - which is typically a quite demanding issue in space - has significantly reduced requirements and is even not necessary [59–62].

### *4.2 Lidar receiver*

The receiver should consist of a large-aperture telescope and a highly efficient receiving unit for the collection of the elastic and rotational/vibrational Raman signals. In order to have a high impact on weather and climate research, simulations indicate that the use of a telescope with a primary-mirror diameter of 4 m would be advantageous. The development of large-aperture telescopes may consider different technological solutions, as the use of segmented deployable or inflatable optics [63], the former being at present the solution characterized by the highest technological maturity, i.e. the highest technological readiness level. Technological concepts for large aperture, lightweight telescopes for lidar applications using thin deployable active mirrors have been reported by Simonetti *et al*. (2010) [64]. Several glass materials (e.g. Zerodur) have been tested and demonstrated to have the appropriate low weight and thermal stability characteristics for this type of space application. This solution was demonstrated to reach near diffraction-limited performances for telescope apertures not exceeding 0.5 m in diameter [65].

Diffraction-limited performance (surface wave-front error < λ/14 RMS or Strehl ratio > 0.8) is beyond the technical requirements for lidar receivers as telescopes for lidar applications do not need to have astronomical quality. In this respect, it is to be stressed that the quality of the telescope primary mirror is an important driver of the overall weight and cost of a space mission. For the only purpose of photon collection, if imaging capabilities are not required, an optical quality of the telescope primary mirror corresponding to a surface wave-front error of the order of λ RMS is sufficient [66, 67]. This wave-front error value is sensitively larger than the diffraction limit and translates into a RMS wave-front error of ~350 nm. Large aperture primary mirrors (with a total surface of ~10 $m^2$), with adequate rigidity, low weight (primary mirror areal density ~15 $kg/m^2$), high wave-front quality (< λ/3) and sufficient temporal and thermal stability, have been demonstrated to be developable based on the use of segmented mirrors, including a very rigid carbon-fibre composite back-

plane and a thin Zerodur glass shell, supported by a set of high efficiency electromagnetic, actively-controlled actuators [68]. The largest diameter optical telescope presently under development for space deployment is the James Webb Space Telescope, to be launched with an Ariane 5 rocket in October 2018 as part of NASA's Flagship Program [69]. This astronomical quality telescope, with diffraction-limited performances and operating in the visible and near IR, is developed around a 6.5 m diameter segmented primary mirror. The Webb Space Telescope has an architecture similar to the one described above and will represent a benchmark for future developments of large-aperture telescopes for space lidar applications. It is to be pointed out that the implementation of a 4 m-diameter telescope, as the one conceived for the present system, allows reaching a level of measurement accuracy having a maximum impact on NWP and climate research. However, a space-borne Raman lidar including a 2-3 m-diameter telescope would reach a sufficiently high level of accuracy to have an impact on NWP and climate (see more details on this in section 5.2).

Simulations illustrated in the forthcoming sections suggest the use a receiving field-of-view (full width half maximum, FWHM) of 25 μrad, which is the same as considered for ADM-Aeolus. Spectral selection of the collected Raman backscattered signals is proposed to be based on interference filters, whose specifications are reported in the next sub-section. Reported simulations consider photon detection by accumulation charge-coupled devices (ACCDs), as for ADM-Aeolus, with UV quantum efficiencies of 85%.

### *4.3 Interference filter specifications*

In the considered receiver optical layout there is no need for complex Fabry-Perot interferometers or gratings, which can be considered to further suppress daylight background [16, 70]. Such interferometers pose large demands in terms of mechanical and thermal stability.

Interference filters' (IFs) specifications for the different measurement channels have to be properly defined in order to minimize measurement uncertainty and improve performances. The primary parameters to be specified are the centre wavelength, $\lambda$, the bandwidth, $\Delta\lambda$ (full width half maximum, FWHM), the centre wavelength transmission, $T_{\lambda}$, and the out of band transmission, i.e. the transmission outside the filter pass-band spectral region, $T_{\neq\lambda}$, and at $\lambda_0$, $T_{\lambda_0}$) (see [29] for an overview). Values for the centre wavelengths for the considered IFs were already specified in section 2.

Specifications of the IF for the selection of the water vapour vibrational Raman lidar signal are taken from [25]. These specifications were defined with the purpose to minimize solar background radiation passing through the filter and, consequently, maximize day-time performances. The centre wavelength is $\lambda_{H_2O}$ = 407.50 nm, the bandwidth is $\Delta\lambda_{H_2O}$ = 0.25 nm and the out of band transmissions $T_{\neq\lambda_{H_2O}}$ and $T_{\lambda_0}$ are smaller than $10^{-6}$ and $10^{-10}$, respectively. The centre wavelength transmission $T_{\lambda_{H_2O}}$ is equal to 80% [71]. Thin-film, ultra-narrow band-pass IFs with values of $T_{\lambda_{H_2O}} \geq 95\%$ have been demonstrated to be feasible [72]. It is to be pointed out that the use of narrow-band interference filters for the selection of the $H_2O$ lidar signals imposes a proper accounting for the temperature dependence of $H_2O$ Raman scattering lines. For the considered filter specifications, the magnitude of this effect varies from 0 to 2% in the temperature range observed from surface up to 10 km [37]. This height-dependent systematic uncertainty source can be properly corrected for based on the simultaneous temperature profile measurements provided by the lidar; these allow determining the term $f_2(z)$ in expression (2), with a residual uncertainty affecting water vapour mixing ratio measurements after correction estimated to not exceed 0.5%.

For what concerns the IFs used for the selection of the low- and high-quantum number rotational Raman signals, in the present simulations we are considering the specifications

reported by Hammann and Behrendt (2015) [29]. The selected centre wavelength are $\lambda_{LoJ}$ = 354.36 nm and $\lambda_{HiJ}$ = 353.29 nm, the bandwidth are $\Delta\lambda_{LoJ}$ = 0.30 nm and $\Delta\lambda_{HiJ}$ = 0.50 nm, the centre wavelength transmissions are $T_{\lambda_{LoJ}}$ = 60% and $T_{\lambda_{HiJ}}$ = 80%, respectively. The out of band transmissions $T_{\neq\lambda_{LoJ/HiJ}}$ and $T_{\lambda_0}$ for both filters are smaller than $10^{-6}$ and $10^{-8}$, respectively. These values $T_{\neq\lambda_{LoJ/HiJ}}$ and $T_{\lambda_0}$ have been demonstrated to be achievable based on the implementation of interference-filter polychromators [40]. The specifications of the IF used for the spectral selection of elastic backscatter signals are also taken from [25]. Specifically, the centre wavelength is $\lambda_0$ = 354.71 nm, the bandwidth is $\Delta\lambda_0$ = 0.50 nm, the centre wavelength transmission is $T_{\lambda_0}$ = 80%, and the out of band transmission $T_{\neq\lambda_0}$ is smaller than $10^{-6}$. The specifications of all IFs are included in Table 1.

**Table 1. Specifications of the interference filters considered in the simulations.**

| Selected signal | | Centre wavelength $\lambda$ (nm) | Bandwidth $\Delta\lambda$, FWHM (nm) | Centre wavelength transmission $T_\lambda$ (%) | Outside pass-band transmission, $T_{\neq\lambda}$ | Transmission at $\lambda_0$, $T_{\lambda_0}$ |
|---|---|---|---|---|---|---|
| $H_2O$ Raman | | 407.50 | 0.25 | 80 | $< 10^{-6}$ | $< 10^{-10}$ |
| Low-J rot. Raman | | 354.36 | 0.30 | 60 | $< 10^{-6}$ | $< 10^{-8}$ |
| High-J rot. Raman | | 353.29 | 0.50 | 80 | $< 10^{-6}$ | $< 10^{-8}$ |
| Elastic at $\lambda_0$ | | 354.71 | 0.50 | 80 | $< 10^{-6}$ | |

### *4.4 Possible sub-system trade-offs*

Raman lidar is a scalable technique, i.e. the random uncertainty affecting the measurements can be reduced/increased by improving/degrading specific instrumental parameters. Both $\Delta x_{H_2O}(z)$ and $\Delta T$ are proportional to:

$$\sqrt{P_0 A_{tel} \eta \Delta x \Delta z} \tag{18}$$

with $\Delta x$ being the horizontal resolution of the measurements, while all other parameters have been already defined above. $\Delta x$ is proportional to the measurement integration time, $\Delta t$, through the expression: $\Delta x = v \cdot \Delta t$, with $v$ being the satellite speed (7 km/s in case of a sun synchronous low-Earth orbit). Expression (18) implies that the same measurement precision can be achieved by keeping constant the power-telescope aperture product $P_0 \times A_{tel}$ and trading-off between $P_0$ and $A_{tel}$. Specifically, a smaller telescope area can be considered in combination with a larger power laser source, preserving same measurement precision. For example, same values of $\Delta x_{H_2O}(z)$ and $\Delta T$ can be achieved combining a 2.8 m diameter telescope with a 500 W laser source as an alternative to the presently considered solution of a 4 m diameter telescope in combination with a 250 W laser source. This option would be preferred in case future technological studies will indicate that weight constraints for the considered payload are more stringent than the electrical power and laser power scaling constraints.

Optics EXPRESS

## 5. Simulations

### *5.1 Daylight background computation*

In order to quantify the background radiation collected in the different lidar channels, several considerations have to be made on the selected satellite orbit. The selected sun-synchronous dawn-dusk orbit is characterized by solar zenith angle (SZA) values always exceeding 65° at all latitude and seasons (Fig. 1). More specifically, SZA values exceed 70° in the latitudinal interval 60°S-60°N; in Tropical regions, i.e. in the latitudinal interval 23°26′13.3″N-23°26′13.3″S, values of SZA are found to always exceed 82°, while in Mid-Latitude regions (latitudinal intervals: 23°26′13.3″-66°33′39”N and 23°26′13.3″-66°33′39”S), values of SZA exceed 68°.

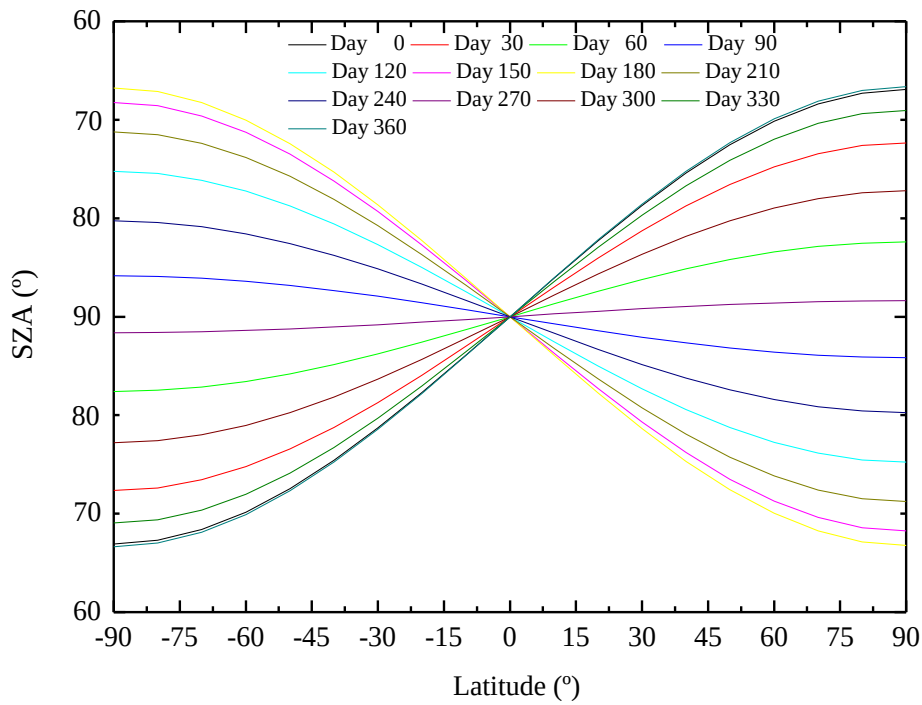


Fig. 1. Variability of the zenith angle, SZA, as a function of latitude for different days of the year. Days are expressed with the Julian calendar.

In the simulations we considered daylight background signal corresponding to the maximum and minimum values of SZA encountered in each latitudinal region. Thus, simulated night-time and daytime performances can be considered as best and worst case scenarios, respectively, with measurement uncertainty at any time and location always in between those obtained with the two SZA values. We recall that, for the purpose to simulate system performance in extreme conditions, i.e. in the presence of strong humidity and temperature gradients, we are also considering the radiosonde profiles used in [10], occurred at 11:30 UTC on 21 September 2007 during the ARM Mobile Facility deployment in the Black Forest (Lat:48.64°N, Long:8.06°E) in southwest Germany. The corresponding maximum and minimum values of SZA encountered at this latitude and day of the year are considered from Fig. 1. Daylight background signal has been estimated for all lidar receiving wavelengths, i.e. $\lambda_{0}$, $\lambda_{LoJ}$, $\lambda_{HiJ}$ and $\lambda_{H_2O}$.

Optics EXPRESS

As already specified above, in estimating the Earth surface contribution to daylight background signals, a default value for the Earth surface albedo of 0.3 has been considered. In estimating the cloud contribution to daylight background signals, specific cloud types (and corresponding cloud reflectivity values) and altitudes were considered (see more detail in section 5.3).

### *5.2 Measurement precision in clear-sky conditions*

The considered system design includes an acquisition system sampling four single-shot lidar signals ( $P_{H_2O}(z)$, $P_{loJ}$(z), $P_{HiJ}$(z) and $P_{\lambda_0}(z)$ ) for each laser shot. In 1 s, these four signals are sampled 100 times each at a laser repetition rate of 100 Hz. Lidar echoes are sampled with a typical time resolution of 50-100 ns, corresponding to a vertical bin size of 7.5-15 m. Horizontal and vertical averaging of the signals is required to reduce signal statistical uncertainties. In order to have a maximum impact on the weather and climate research applications identified in Section 1, vertical and horizontal resolutions of 200 m and 50 km, respectively, are considered in the simulations. As the satellite speed for an orbiting altitude of 450 km is 7 km/s, a horizontal resolution of 50 km is obtained with an integration time of 7.14 s, which corresponds to a summation over 714 consecutive lidar echoes, each one separated from the previous by 70 m due to the 100 Hz repetition rate of the laser. Analogously, a vertical resolution of 200 m is obtained with a vertical integration over 13-26 range bins. Different averaging approaches can be applied, e.g. typically a running or gliding average.

Figure 2 illustrates the vertical profiles of $\Delta x_{H_2O}(z)/x_{H_2O}(z)$ for the US Standard Atmosphere 1976 and the Tropical and Mid-Latitude Summer/Winter atmospheric reference models. The figure convers the height interval up to 5 km. As specified above, values of SZA for a sun synchronous dawn-dusk orbit always exceed 65° at all latitude and seasons, so values of $\Delta x_{H_2O}(z)/x_{H_2O}(z)$ for the US Standard Atmosphere 1976, which is a globally and yearly averaged atmospheric model, are always in between those obtained for SZA = 90° (minimum uncertainty) and SZA = 65° (maximum uncertainty). Values of SZA always exceed 82° in Tropical regions, so that in these regions $\Delta x_{H_2O}(z)/x_{H_2O}(z)$ is always in between the values obtained for SZA = 90° and SZA = 82°; finally, values of SZA always exceed 68° in Mid-Latitude regions, with values of $\Delta x_{H_2O}(z)/x_{H_2O}(z)$ always in between those obtained for SZA = 90° and SZA = 82°.

Figure 2(a) reveals that values of $\Delta x_{H_2O}(z)/x_{H_2O}(z)$ for the US Standard Atmosphere are in the range 3-20% up to 2.2 km and are smaller than 50% up to 4 km. For a Tropical atmosphere values of $\Delta x_{H_2O}(z)/x_{H_2O}(z)$ are in the range 2-20% up to 5.4 km and are smaller than 50% up to 7.2 km (Fig. 2(b)), while for a Mid-Latitude Summer atmosphere values of $\Delta x_{H_2O}(z)/x_{H_2O}(z)$ are in the range 2-20% up to 3.8 km and are smaller than 50% up to 5.6 km (Fig. 2(c)). Finally, for a Mid-Latitude Winter atmosphere values of $\Delta x_{H_2O}(z)/x_{H_2O}(z)$ are in the range 4-30% up to 2.2 km and are smaller than 50% up to 3.6 km (Fig. 2(d)). These results are summarized in Table 2, which is listing measurement specifications for all measured atmospheric variables.

Optics EXPRESS

**Table 2. Measured atmospheric variables and their specifications. Precisions are altitude and latitude dependent. MLS and T stand for mid-latitude summer and tropical climatologies, respectively. The upper troposphere-lower stratosphere (UTLS) is intended to extend up to 18-20 km.**

| Variable | Coverage and comments | Resolution (vert/hor) | Precision |
|---|---|---|---|
| Water vapor mixing ratio | Global, nadir from ground up to 5.4 km (T) and 3.8 km (MLS) | 200 m / 50 km | 2-20% |
| Temperature | Global, nadir from ground up to UTLS | 200 m / 50 km | 0.4-1 K |
| Relative humidity | Global, nadir from ground up to 5.3 km (T) and 3.7 km (MLS) | 200 m / 50 km | 2-20% |
| PBL height | Global, nadir | 100 m / 5 km | 100 m |
| Particle backscatter & extinction | Global, nadir, from ground up to 2 km | 50-100 m / 10-50 km | 1-3% & 3-20% |
| Cloud distribution | Cloud top height, base height of opt. thin clouds | 50-100 m / 5 km | 50-100 m |
| Cloud optical depth | Opt. thin mid-level and cirrus clouds | 50 km | 5% |

Optics EXPRESS

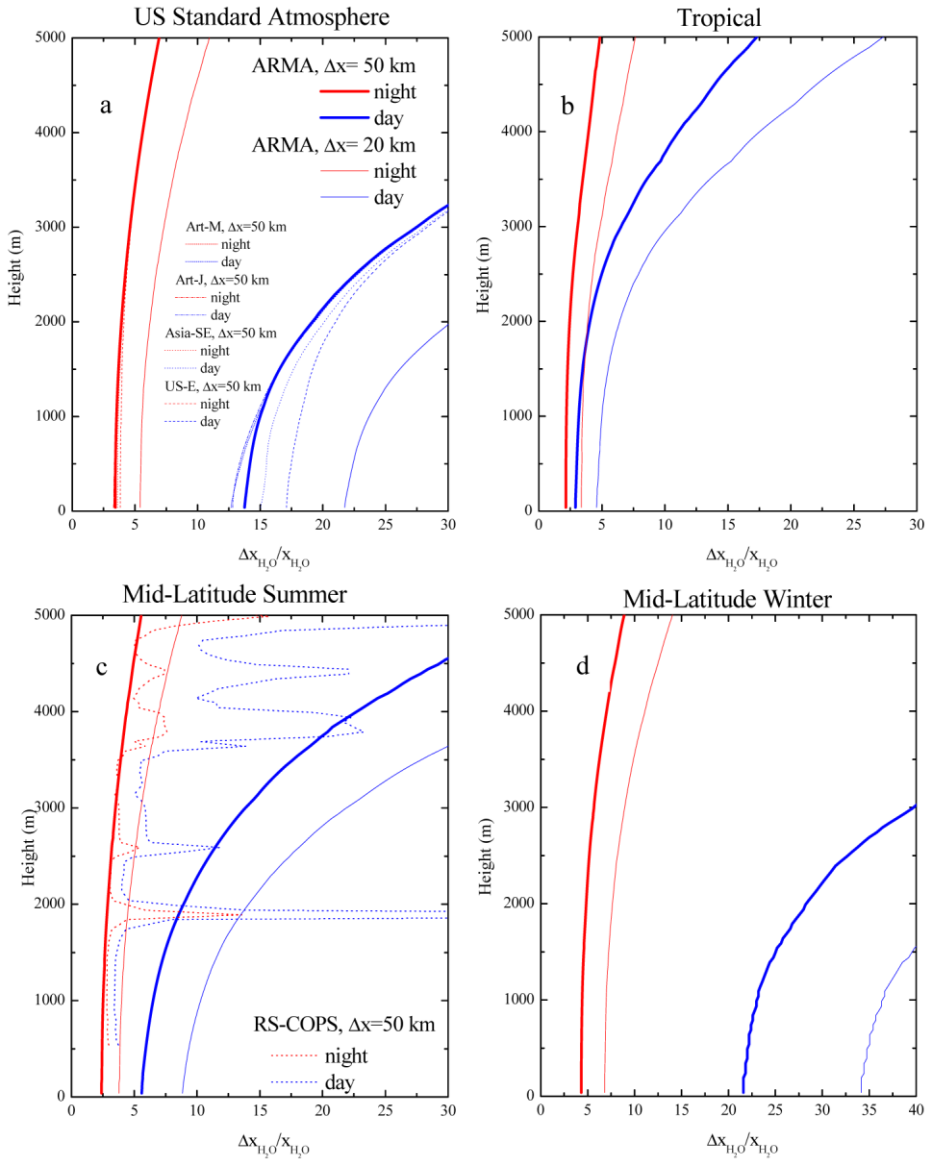


Fig. 2. Vertical profiles of $\Delta x_{H_2O}(z)/x_{H_2O}(z)$ for the US Standard Atmosphere 1976 (panel a), the Tropical (panel b) and Mid-Latitude Summer/Winter atmospheric reference models (panel c and d, respectively). Daytime performance is simulated considering a minimum SZA value of 65°, 82° and 68° for the US Standard Atmosphere 1976, the Tropical and the Mid-Latitude model, respectively. Thin lines represent a horizontal resolution of 20 km, while bold lines represent a horizontal resolution of 50 km. In panel a) simulations performed with aerosol data from [50] are also included (Eastern US, 31–41 °N, 95–75 °W, during July 2006–2011, South-Eastern Asia, 1–19 °N, 90–110 °E, August 2006–2011, Arctic, 61–82 °N, January 2007–2011and March 2007–2011), all with a horizontal resolution of 50 km.

In all panels of Fig. 2 results obtained considering a horizontal resolution of 20 km are also illustrated. These results allow revealing the extraordinary instrumental performances within the PBL and in the transition region to the free troposphere, even at this improved horizontal resolution, with the mean value of $\Delta x_{H_2O}(z)/x_{H_2O}(z)$ up to 2 km being 17.2, 5.0, 8.7 and 25% for the US Standard Atmosphere 1976, the Tropical and the Mid-Latitude

Summer/Winter atmospheric reference models, respectively. Figure 2(c) also include the simulated profile of $\Delta x_{H_2O}(z)/x_{H_2O}(z)$ in the extreme conditions represented by the selected radiosonde profiles (Black Forest, 11:30 UTC on 21 September 2007) characterized by the presence of a number of dry lamina and a temperature inversions in the lower troposphere. Values of $\Delta x_{H_2O}(z)/x_{H_2O}(z)$ up to 100% are present within the dry lamina, where values of RH and $x_{H_2O}(z)$ are very small (< 2% and < 0.15 g kg$^{-1}$, respectively). Figure 2(a) also includes the simulated profile of $\Delta x_{H_2O}(z)/x_{H_2O}(z)$ obtained considering the aerosol backscatter/extinction climatological analysis reported by [50]. The effect of considering different aerosol models/climatologies is assessed. Results reveal that daytime values of $\Delta x_{H_2O}(z)/x_{H_2O}(z)$ obtained using the Eastern US and South-Eastern Asia summer climatological data are 2-3% larger than those obtained with the ARMA aerosol model, while those obtained using the Arctic winter climatological data are 1-2% smaller than those obtained with the ARMA aerosol model.

Figure 3 illustrates the vertical profiles of $\Delta T$ for the US Standard Atmosphere 1976 and the Tropical and Mid-Latitude Summer/Winter atmospheric reference models. The figure convers the height interval up to 20 km. Values of $\Delta T$ up to 20 km are smaller than 0.8 K for the Tropical model, smaller than 1.2 K for the US Standard Atmosphere and the Mid-Latitude Winter model and smaller than 1.1 K for the Mid-Latitude Summer model. For all considered atmospheric models, $\Delta T$ is in the range 0.40-0.75 K in the height interval from the surface up to 15 km. Additionally, for all considered models $\Delta T$ is found to decrease with height up to approx. 10 km, where minimum values are reached ($\Delta T_{min}$ = 0.4-0.50 K at 9 km for the US Standard Atmosphere, $\Delta T_{min}$ = 0.45-0.50 K at 11 km for the Tropical model, $\Delta T_{min}$ = 0.45-0.50 K at 10 km for the Mid-Latitude Summer model and $\Delta T_{min}$ = 0.40-0.50 K at 8 km for the Mid-Latitude Winter model). Also in the case of temperature measurements, it is worth focusing on the excellent performances within the PBL and in the transition region to the free troposphere. Mean value of $\Delta T$ is 0.8-0.9 K for all considered atmospheric models when considering a horizontal resolution of 20 km. Figure 3(c) also include the simulated profile of $\Delta T$ for the selected radiosonde profiles, characterized by the presence of temperature inversions and strong gradients in the lower troposphere. The profile of $\Delta T$ is not affected by the presence of these gradients, with values being even smaller than those typically found in the Mid-Latitude Summer atmosphere, as result of the smaller background signal at this latitude and season. Figure 3(a) also includes the simulated profile of $\Delta T$ obtained considering the aerosol backscatter/extinction climatological analysis reported by [50], with results revealing that values of $\Delta T$ obtained using the Eastern US and South-Eastern Asia summer climatological data are 0.05-0.10 K larger than those obtained with the ARMA aerosol model, while those obtained using the Arctic winter climatological data are up to 0.05 K smaller than those obtained with the ARMA aerosol model.

Figure 4 illustrates the vertical profiles of the random uncertainty affecting *RH* measurements. Values of $\Delta RH(z)/RH(z)$ for the US Standard Atmosphere are in the range 3-20% up to 2.1 km and are smaller than 50% up to 3.9 km (Fig. 4(a)). For a Tropical atmosphere values of $\Delta RH(z)/RH(z)$ are in the range 2-20% up to 5.4 km and are smaller than 50% up to 7.2 km (Fig. 4(b)). For a Mid-Latitude Summer atmosphere values of $\Delta RH(z)/RH(z)$ are in the range 2-20% up to 3.7 km and are smaller than 50% up to 5.6 km (Fig. 4(c)), while for a Mid-Latitude Winter atmosphere values of $\Delta RH(z)/RH(z)$ are in the range 4-20% up to 2.1 km and are smaller than 50% up to 3.5 km. It is to be pointed out that, for all considered atmospheric models, in the lower levels up to approx. 5 km values of $\Delta RH(z)/RH(z)$ are slightly larger than those of $\Delta x_{H_2O}(z)/x_{H_2O}(z)$ as in fact in the lower levels the contribution to $\Delta RH(z)/RH(z)$ from water vapour mixing ratio and temperature measurement uncertainties are comparable; on the contrary, deviations between

Optics EXPRESS

$\Delta RH(z)/RH(z)$ and $\Delta x_{H_2O}(z)/x_{H_2O}(z)$ are negligible above 5 km as a result of the fact that the contribution to $\Delta RH(z)/RH(z)$ from $\Delta T$ is much smaller than the contribution from $\Delta x_{H_2O}(z)/x_{H_2O}(z)$. When considering a horizontal resolution of 20 km, a mean value for $\Delta RH(z)/RH(z)$ up to 2 km of 17.9, 6.5, 10.6 and 27.6% is estimated for the US Standard Atmosphere 1976, the Tropical and the Mid-Latitude Summer/Winter atmospheric reference models, respectively, once again revealing extraordinary performance within the PBL and in the transition region to the free troposphere

Figures 5 and 6 illustrate the vertical profiles of $\Delta\beta_{\lambda_0}^{par}(z)/\beta_{\lambda_0}^{par}(z)$ and $\Delta\alpha_{\lambda_0}^{par}(z)/\alpha_{\lambda_0}^{par}(z)$, respectively, for the considered atmospheric models. For all considered atmospheric models, values of $\Delta\beta_{\lambda_0}^{par}(z)/\beta_{\lambda_0}^{par}(z)$, both in nighttime and daytime, are smaller than 3% up to approx. 2 km, smaller than 10% up to approx. 2.5 km and reach 100% in the altitude range 4.7-5.2 km, again revealing the excellent performance within the PBL and in the transition region to the free troposphere. It is to be noticed that for all considered atmospheric models $\Delta\beta_{\lambda_0}^{par}(z)/\beta_{\lambda_0}^{par}(z)$ reaches 100% around the same altitude where $\beta_{\lambda_0}^{par}(z)$ gets smaller $5 \times 10^{-9}$ $m^{-1}$ $sr^{-1}$. This effect is primarily associated with the selected clear-air aerosol model. As specified above, the ARMA model includes a mid- and upper-tropospheric aerosol layer, with values of $\beta_{\lambda_0}^{par}(z)$ slowly decreasing with altitude down to $2 \times 10^{-9}$ $m^{-1}$ at the tropopause. Consequently, the value $5 \times 10^{-9}$ $m^{-1}$ $sr^{-1}$ can be considered as a sensitivity limit for $\beta_{\lambda_0}^{par}(z)$ measurements and aerosol layers characterized by $\beta_{\lambda_0}^{par}(z)$ values larger than this limit are measured with smaller uncertainties even when appearing at higher altitudes. Consequently, a sensitivity limit as an alternative to an altitude coverage range should be considered when assessing the system performance in terms of particle backscatter measurements.

$\Delta\alpha_{\lambda_0}^{par}(z)/\alpha_{\lambda_0}^{par}(z)$ is smaller than 20% up to approximately 2.0 km and smaller than 100% up to approximately 2.5 km, both in nighttime and daytime. Similar considerations as for $\Delta\beta_{\lambda_0}^{par}(z)/\beta_{\lambda_0}^{par}(z)$ also apply to $\Delta\alpha_{\lambda_0}^{par}(z)/\alpha_{\lambda_0}^{par}(z)$. In this respect it is to be specified that for all considered atmospheric models $\Delta\alpha_{\lambda_0}^{par}(z)/\alpha_{\lambda_0}^{par}(z)$ reaches 100% around an altitude of 2.3 km, where values of $\alpha_{\lambda_0}^{par}(z)$ get smaller than $2.5 \times 10^{-7}$ $m^{-1}$, this latter value being considerable as a sensitivity limit for particle extinction measurements. While the value $2.5 \times 10^{-7}$ $m^{-1}$ represents a sensitivity limit for particle extinction measurements, values typically observed within clouds are much larger and are consequently characterized by much smaller uncertainties. E.g., a precision of ≤ 5% is reached for a particle extinction coefficient of $\geq 5 \times 10^{-6}$ $m^{-1}$ which can be regarded as a typical value within a cloud.

Optics EXPRESS

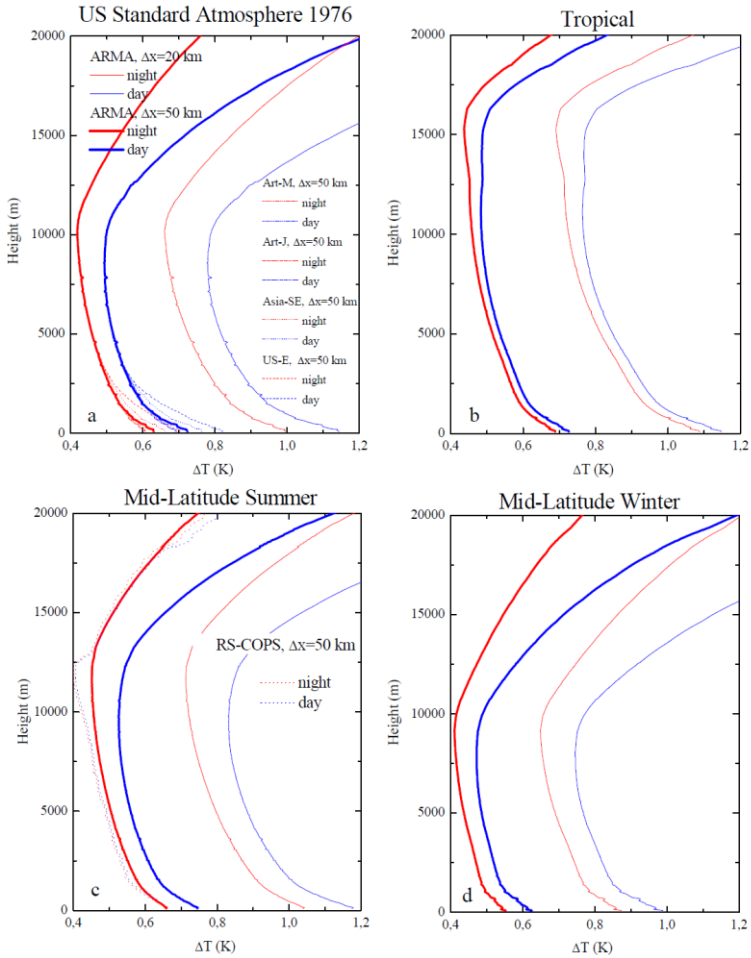


Fig. 3. Vertical profiles of $\Delta T$ for the US Standard Atmosphere 1976 (panel a), the Tropical (panel b) and Mid-Latitude Summer/Winter atmospheric reference models (panel c and d, respectively). Daytime performance is simulated considering a minimum SZA value of 65°, 82° and 68° for the US Standard Atmosphere 1976, the Tropical and the Mid-Latitude model, respectively. Thin lines represent a horizontal resolution of 20 km, while bold lines represent a horizontal resolution of 50 km. In panel a) simulations performed with aerosol data from [50] are also included (Eastern US, 31–41 °N, 95–75 °W, during July 2006–2011, South-Eastern Asia, 1–19 °N, 90–110 °E, August 2006–2011, Arctic, 61–82 °N, January 2007–2011and March 2007–2011), all with a horizontal resolution of 50 km.

As already mentioned above, the proposed system can independently measure the true PBL depth over land and the oceans. This is a unique feature of this instruments, as this derivation – which is based on a true simultaneous and collocated temperature profiles - is not possible with any other instrumentation. Accurate PBL depth measurements have been verified to be feasible with vertical and horizontal resolutions of 200 m and 50 km, respectively, and an accuracy of 200 m. However, as the random uncertainty affecting temperature measurements is quite small in the upper portion of the PBL, PBL depth measurements can also be obtained from higher resolution temperature profile measurements, with simulations confirming the possibility to achieve vertical and horizontal resolutions as small as 100 m and 5 km, respectively.

Results illustrated in the present section should be evaluated with regard to the considerations reported in section 4.4, i.e. recalling that the Raman lidar technique is scalable and measurement precision can be reduced by downsizing specific instrumental parameters. In this respect it is to be pointed out that a demanding technological achievement of this

Optics EXPRESS

mission design is represented by the development of the space-qualified 4 m diameter telescope. With regard to this critical point, it is to be specified that a strong impact on NWP and climate applications can already be achieved with the measurements carried out by a space Raman lidar with a 2 m-diameter telescope. In fact, as it can be inferred from expression (18), both $\Delta x_{H_2O}(z)$ and $\Delta T$ linearly scale with the telescope diameter, and therefore a 50% reduction in telescope diameter translates into a 50% reduction for both $\Delta x_{H_2O}(z)$ and $\Delta T$. Consequently, based on the results reported above, we can infer that values of $\Delta x_{H_2O}(z)/x_{H_2O}(z)$ are smaller than 40% up to 2.2 km, 5.4 km, 3.8 km and 1.0 km for the US Standard Atmosphere 1976, the Tropical and Mid-Latitude Summer/Winter atmospheric reference models, respectively, while values of $\Delta T$ are smaller than 2 K up to approximately 20 km and in the range 0.8-1.5 K up to 15 km for all considered atmospheric models.

To conclude this section, we need to recall that, analogously to any other active remote sensing instrument, the vertical resolution of Raman lidar measurements is well defined and determined from the sampling resolution of the acquisition system, with the maximum resolution being given by the laser pulse duration. An additional advantage of the proposed system when compared with traditional passive remote sensing systems is the larger accuracy and vertical resolution, as well as the detailed characterization of the random uncertainty affecting the measurement in each single vertical range bin and for each individual profile, which is determined from the number of detected signal photons through the application of Poisson statistics, via error propagation (see section 3). This latter advantage is expected to have a strong positive impact on numerical weather prediction, exploiting the potential of the measured profiles in weather forecast models through data assimilation [73]. Several studies confirmed that the quantification of the random uncertainty through Poisson statistics represents a good estimate of the total random uncertainty (e.g., [21]).

Optics EXPRESS

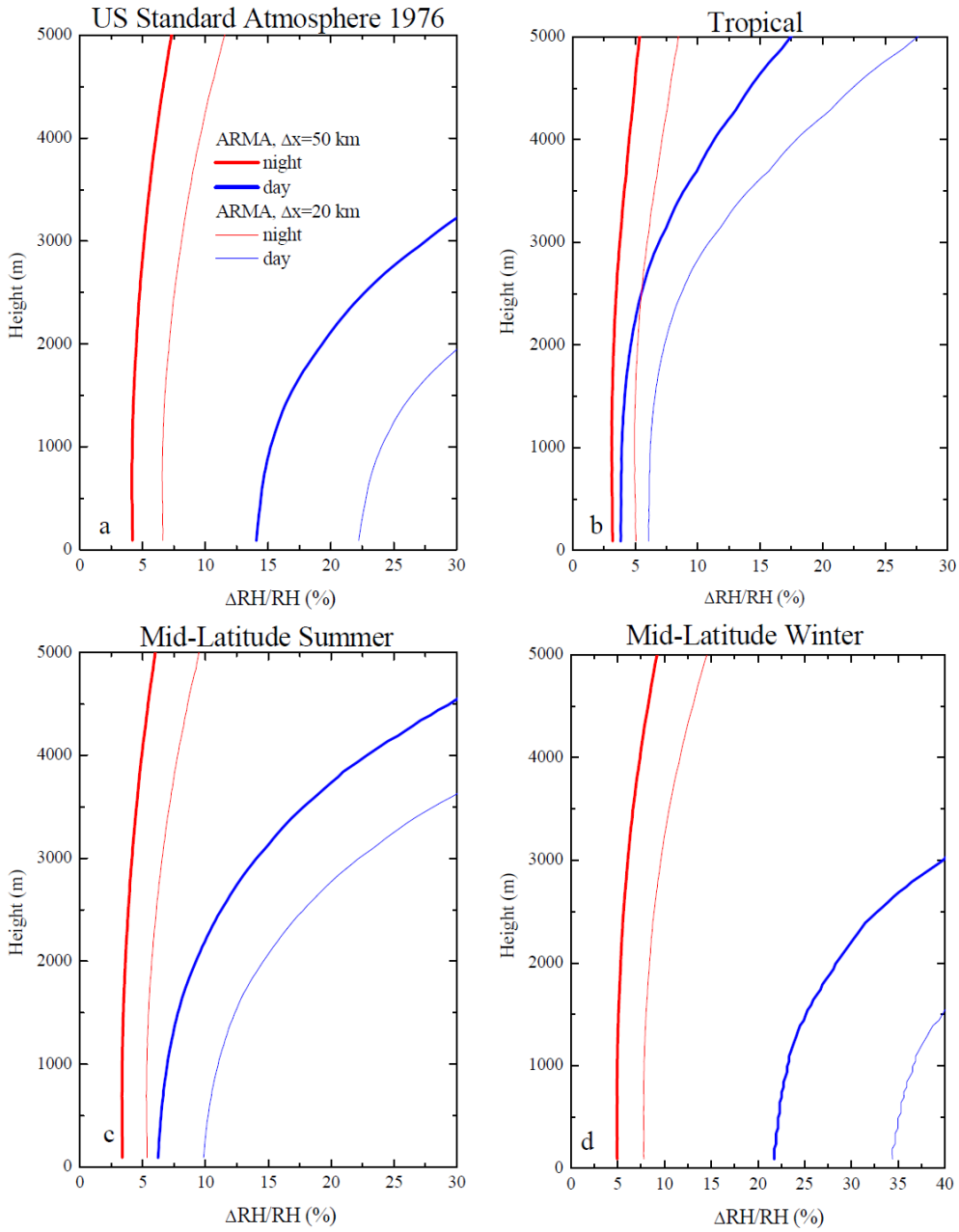


Fig. 4. Vertical profiles of *ΔRH(z)/RH(z)* for the US Standard Atmosphere 1976 (panel a), the Tropical (panel b) and Mid-Latitude Summer/Winter atmospheric reference models (panel c and d, respectively). Daytime performance is simulated considering a minimum SZA value of 65°, 82° and 68° for the US Standard Atmosphere 1976, the Tropical and the Mid-Latitude model, respectively. Thin lines represent a horizontal resolution of 20 km, while bold lines represent a horizontal resolution of 50 km.

Optics EXPRESS

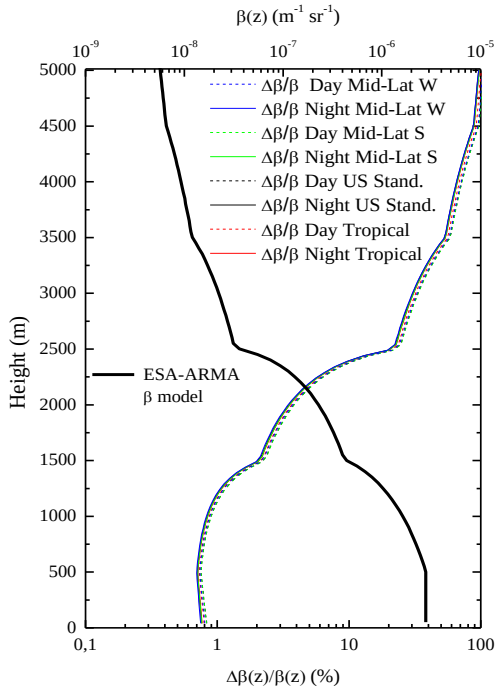


Fig. 5. Vertical profiles of $\Delta\beta_{\lambda_0}^{par}(z)/\beta_{\lambda_0}^{par}(z)$ for the for the US Standard Atmosphere 1976, the Tropical and Mid-Latitude Summer/Winter atmospheric reference models. The ESA-ARMA aerosol backscatter model is also introduced in the figure.

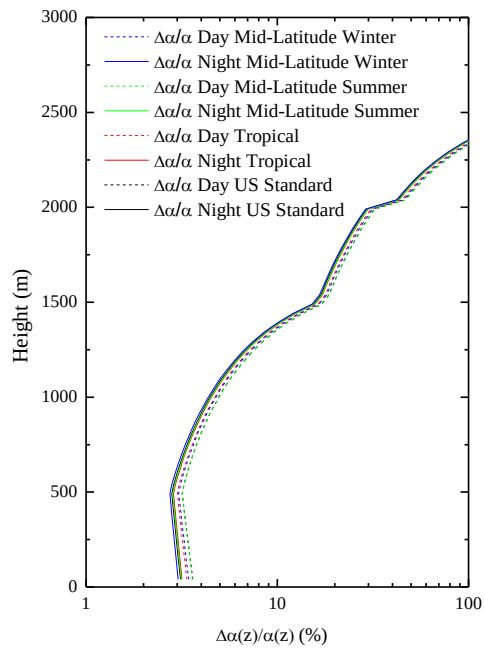


Fig. 6. Vertical profiles of $\Delta\alpha_{\lambda_0}^{par}(z)/\alpha_{\lambda_0}^{par}(z)$ for the for the US Standard Atmosphere 1976, the Tropical and Mid-Latitude Summer/Winter atmospheric reference models.

Optics EXPRESS

### 5.3 Measurement precision in cloudy conditions

The effect of clouds on measurement precision has been assessed, with a specific focus on cirrus and mid-level clouds. It has been demonstrated that systematic uncertainties affecting temperature and water vapor measurements in clouds are completely removed when selecting interference filters for the Raman channels with sufficiently high blocking for the elastic backscatter signal [16, 18, 38]. However, cloud extinction reduces the intensities of the Raman signals, thus increasing measurement random uncertainty. Additionally, in the presence of clouds, daytime background signal may increase as clouds backscatter background light more efficiently than a pure molecular atmosphere.

For the purpose of these simulations, we considered a cirrus layer with a Gaussian-shape profile, with a peak backscattering ratio at 354.7 nm at 9 km equal to 8 and a vertical extent (FWHM) of 180 m. The cirrus cloud optical thickness at 354.7 nm is taken equal to 0.3, while its lidar ratio at this same wavelength is taken equal to 30 sr [74]. More typical lidar ratio values for cirrus clouds are in the range 15-20 sr, but the consideration of a value of 30 sr generates an enhancement of cloud extinction, and consequently simulates a worst case scenario, thus leading to a more prudential assessment of the system performance. A mid-level (altostratus) Gaussian-shaped cloud layer is also considered, with a peak backscattering ratio of 4 at 3 km, a vertical extent (FWHM) of 180 m, an optical thickness of 0.3 and a lidar ratio of 30 sr. A more typical lidar ratio value for altostrati is ~18 sr [75], but, again, the consideration of the upper limit value of 30 sr allows to obtain a more prudential assessment of the system performance. Since multiple scattering reduces the effects of cloud extinction, the present simulations represent measurement performances with an effective cloud optical thickness up to a factor of 2 larger than the values considered above [76]. The effect of clouds has been accounted for in the determination of both lidar backscatter and background signals. For the calculation of background signals, estimates of cloud reflectivity are required, as in fact a cloud contribution associated with solar radiation reflection by clouds is included in these background signals. In these simulations we considered a cirrus cloud reflectivity of 0.05 and an altostratus reflectivity of 0.64 [16, 77].

Figure 7 shows the model particle backscattering coefficient profile at 354.7 nm, which includes both the aerosol contribution (from the ESA median model) and the two Gaussian-shape cloud layers.

Optics EXPRESS

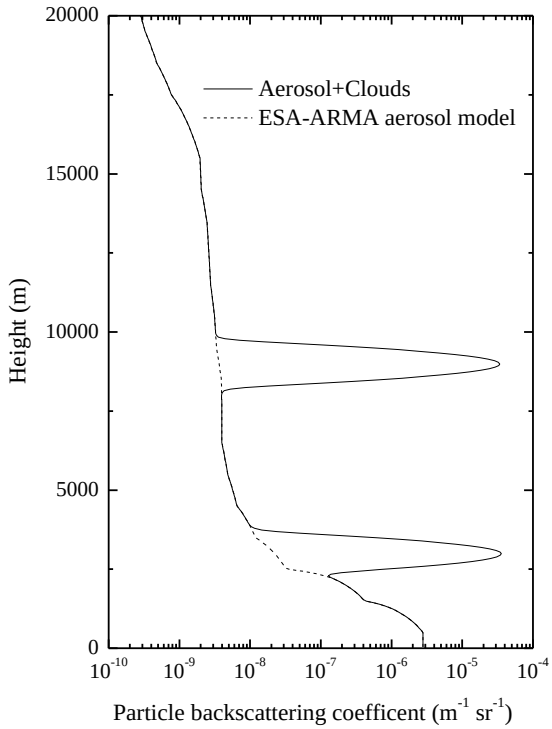


Fig. 7. Vertical profile of the model particle backscattering coefficient profile at 354.7 nm considered in the simulations; the profile includes both an aerosol contribution (from the ESA median model) and the two Gaussian-shape cloud layers.

Figure 8 illustrates the vertical profiles of $\Delta x_{H_2O}(z)/x_{H_2O}(z)$ in cloudy conditions for the US Standard Atmosphere 1976, the Tropical and Mid-Latitude Summer/Winter atmospheric reference models. Two scenarios are considered in each figure, i.e. the presence of the cirrus cloud only and the presence of both the cirrus and the mid-level cloud. In the presence of the cirrus cloud layer only, values of $\Delta x_{H_2O}(z)/x_{H_2O}(z)$ are smaller than 50% up to 2.9, 5.7, 4.3 1.7 km for the US Standard Atmosphere 1976, the Tropical and Mid-Latitude Summer/Winter atmospheric reference models, respectively. In the presence of both the cirrus and the mid-level cloud layers, values of $\Delta x_{H_2O}(z)/x_{H_2O}(z)$ are smaller than 50% up to 5.6 and 3.8 km for the Tropical and Mid-Latitude Summer atmospheric reference models, respectively. Values of $\Delta x_{H_2O}(z)/x_{H_2O}(z)$ are smaller than 100% only up to 1.3 km for the US Standard Atmosphere 1976, while they always exceed 100% for the Mid-Latitude Winter atmospheric reference model.

Figure 9 illustrates the vertical profiles of $\Delta T$ in cloudy conditions for the US Standard Atmosphere 1976, the Tropical and Mid-Latitude Summer/Winter atmospheric reference models. In the presence of the cirrus cloud layer only, $\Delta T$ is smaller than 1.2 K up to 20 km for all considered atmospheric models, while in the presence of both the cirrus and the altostratus cloud layers, $\Delta T$ is smaller than 1.2 K above the altostratus up to 18-20 km, while it is in the range 1.5-3.2 K below the altostratus for all considered atmospheric models. These results confirm that temperature measurements are possible below cirrus and altostratus clouds with an optical thickness not exceeding 0.6, with NWP and climate research observational requirements identified in section 1 fulfilled above and below thin cirrus clouds with an optical thickness of 0.3.

Optics EXPRESS

### 5.4 Assessment of systematic uncertainty sources

Another important systematic uncertainty source traditionally affecting water vapour Raman lidar measurements is associated with the use of narrow-band interference filters for the selection of the $H_2O$ Raman signals, which requires for a proper accounting of the temperature dependence of water vapour roto-vibrational Raman scattering. This height-dependent systematic uncertainty can be properly corrected using simultaneous and co-located temperature profile measurements carried out by the lidar, with a residual uncertainty after correction estimated to not exceed 0.5%.

For what concerns the systematic uncertainty sources affecting atmospheric temperature measurements, a bias may occur as a result of small drifts of the laser and/or the IFs' central wavelength. Laser frequency drifts may be associated with short- or long-term temperature changes taking place inside the laser active medium, while filters' position drifts may result from thermal changes in the filter environment. Variations in signal power ratio associated with laser frequency drifts may generate a systematic measurement uncertainty of the order of 0.005 K per 1 K change of the laser active medium temperature [16]. Advances in frequency stabilization techniques achieved in the last decade allow to totally eliminate this residual uncertainty source. Di Girolamo *et al.* (2006) [16] estimated the bias associated with IF thermal drifts to typically not exceed 0.1 K. Short range measurements by ground-based Raman lidar systems are typically affected by a systematic uncertainty resulting from the partial overlap between the laser beam and the receiver field of view, the so-called overlap effect. However, this effect is not affecting space lidar systems as all information of interest for the measurements are contained in the far range portion of the lidar signals, with the short range portion of these signals not being used.

Uncertainties in the determination of the calibration constants may lead to a small residual systematic uncertainty affecting both water vapour and temperature measurements, which can be minimized based on the implementation of an on-orbit calibration procedure and undertaking of a dedicated Cal/Val effort supported by ground-based, airborne and satellite-based measurements, with an approach similar to the one carried out for the ESA mission ADM-Aeolus. In this respect it is to be specified that two height-dependent correction terms $f_1(z)$ and $f_2(z)$ included in the calibration function *K(z)* defined in expression (1) have a negligible variability with time, as long as the a high-frequency stability laser is used (< 50 MHz) and the interference filters are contained in a thermally controlled environment, which is certainly the case for the devices considered in the present mission concept. The residual uncertainty affecting the calibration constants is estimated in what follows.

In order to understand what is the expected range of time variability, both short-term and long-term, of the calibration constants and the level of accuracy of their estimate, we have to refer to the lessons learnt from previous space lidar missions. After more than 10 years of continuous in-orbit operation, the performance of the two-wavelength elastic backscatter lidar CALIOP, deployed on board the CALIPSO satellite, has demonstrated to keep high in the key areas of laser energy and overall long-term stability. In this regard, the calibration coefficient for the 532 nm attenuated backscatter level 1 data, recently re-determined through a revised algorithm (version 4.1 [78]), has been found to keep quite stable with time, with a standard deviation variability of ± 3% over the 8-year period 2009-2016. Fluctuations of this calibration coefficient have been found to be primarily associated with laser energy fluctuations. A long term decreasing trend (0.5%/yr) has also been revealed, likely due to optical component degradation in the receiver [79]. Sharp short term variations of the calibration coefficient (up to 5%) have been found to take place, primarily associated with the bore-sight alignment optimization procedure [78] carried out periodically during the lifetime of the mission.

It is to be specified that the calibration coefficient of an elastic backscatter lidar, like CALIOP, is determined by normalizing within a specific altitude interval the range-corrected

Optics EXPRESS

(gain and energy-normalized) backscatter signals to the expected backscatter signals computed from an atmospheric scattering model. However, fluctuations of the calibration coefficient for an elastic backscatter lidar are typically larger than those characterizing a Raman lidar as in fact the primary atmospheric quantity measured by backscatter lidars, i.e. particle backscattering coefficient, is obtained from a single backscatter lidar signal, while atmospheric quantities measured by Raman lidars (i.e. water vapour mixing ratio, temperature and particle backscattering coefficient) are obtained from the power ratio of two distinct backscatter lidar signals. These two signals ( $P_{H_2O}(z)$ and $P_{ref}(z)$ in the case of water vapour mixing ratio measurements, $P_{loJ}(z)$ and $P_{HiJ}(z)$ in the case of temperature measurements and $P_{\lambda_0}(z)$ and $P_{ref}(z)$ in the case of particle backscatter measurements) are detected by nearby optical channels within a receiver with a very compact optical design. With such a receiver, signal ratioing allows removing most short term fluctuations, as those related to the fluctuations of laser power and to the application of the boresight alignment optimization procedure.

In order to further assure stability to the transmitter-to-receiver alignment, transmitter and receiver will be located on an optical bench manufactured with a material guaranteeing mechanical and thermal stability (for example, a carbon graphite composite as for CALIOP). The laser transmitter assembly has to be mounted on a beam steering system, allowing pointing direction adjustments for optimizing the boresight alignment between the transmitter and receiver [80].

The use of data from a distributed network of ground-based calibration/validation systems would allow validating the calibration constants and contribute in reducing the systematic uncertainty affecting their estimate, thus improving calibration accuracy. For this purpose, sondes hosting reference humidity/temperature sensors could be launched from specific validation sites. Among the reference sensors, the chilled-mirror hygrometer [81] or the cryogenic frost point hygrometer [82] for relative humidity measurements, with a demonstrated percentage accuracy of 2% and 4%, respectively, over the entire range 0-100%, and the thermo capacitive sensor or the platinum resistor sensor for temperature measurements, with a demonstrated accuracy of 0.2 K and 0.1 K, respectively. The use of reference sondes could be integrated with the operation of ground-based water vapour Differential Absorption Lidars (DIALs), which, because of their self-calibrating capability, have been recognized as one of the water vapour reference standards of the World Meteorological Organization (WMO) [83]. The University of Hohenheim ground-based water vapour DIAL is operational with a routine schedule since more than 10 years, with a demonstrated accuracy of 1-3% [84], the major portion of this uncertainty having a spectroscopic origin as in fact water vapour absorption line parameters included in different databases present small differences (1- 2%).

In support of all Cal/Val effort specified above, the implementation of an in-orbit calibration procedure should also be planned. Referring to previous experiences with ground-based systems, a fist-principle calibration procedure based on the use of a calibration lamp (tungsten–halogen lamp) represents a possible option, with a demonstrated capability to continuously monitor the calibration stability, with an accuracy better than 3% [85]. Simeonov [86] claims the possibility to derive the calibration constant with uncertainty better than 0.1% based on the application of a different first principle calibration method, relying on the use of a gravimetrically produced water vapour/air mixture.

Thus, quality measurements as those provided on a routine basis by the University of Hohenheim ground-based water vapour DIAL, in combination with those from the reference sondes involved in the Cal/Val effort, and supported by an in-orbit calibration procedure as those mentioned above, would allow determining and verifying the stability of the calibration constants of the space Raman lidar, with a residual calibration-related uncertainty of 2-4% and 0.2-0.3 K for water vapour mixing ratio and temperature measurements, respectively.

Optics EXPRESS

While we emphasize that the major focus of this mission idea is on the low-mid troposphere and we are confident that most observational requirements for climate research applications would be fulfilled by the proposed system, we certainly realize that a measurement stability of 0.3% per decade needed for the detection of climate signals/trends (GCOS/ESA-CCI [34]) is out of the system capabilities. However, we are also aware that in the forthcoming future a mission like the one reported in this paper could be taken into consideration by International Space Agencies for deployment in space as a technology demonstration mission, having in mind a life-time of 3-5 years for the mission. Only at a later stage, after the successful deployment of this demonstrator, a long-term space mission more focused on scientific objectives would be considered for space implementation.

For what concerns the systematic uncertainty affecting particle backscatter and extinction measurements, it is to be pointed out that the main bias source affecting these measurements is the one associated with the estimate of the differential transmission term. However, because of the vicinity of the laser and reference signal wavelength in the present system setup, this potential bias source has negligible effects on the measurements.

A bias free measurement of the particle backscatter and extinction coefficients translates into a substantial reduction of one of the bias sources traditionally affecting water vapour Raman lidar measurements, i.e. the one associated with the estimate of the differential transmission term. In fact, bias free measurement of the particle backscatter and extinction coefficients can be used to properly estimate the different atmospheric transmission profiles at $\lambda_{H_2O}$ and $\lambda_{ref}$, with a residual uncertainty affecting water vapour mixing ratio measurements not exceeding 0.3-0.5%.

Optics EXPRESS

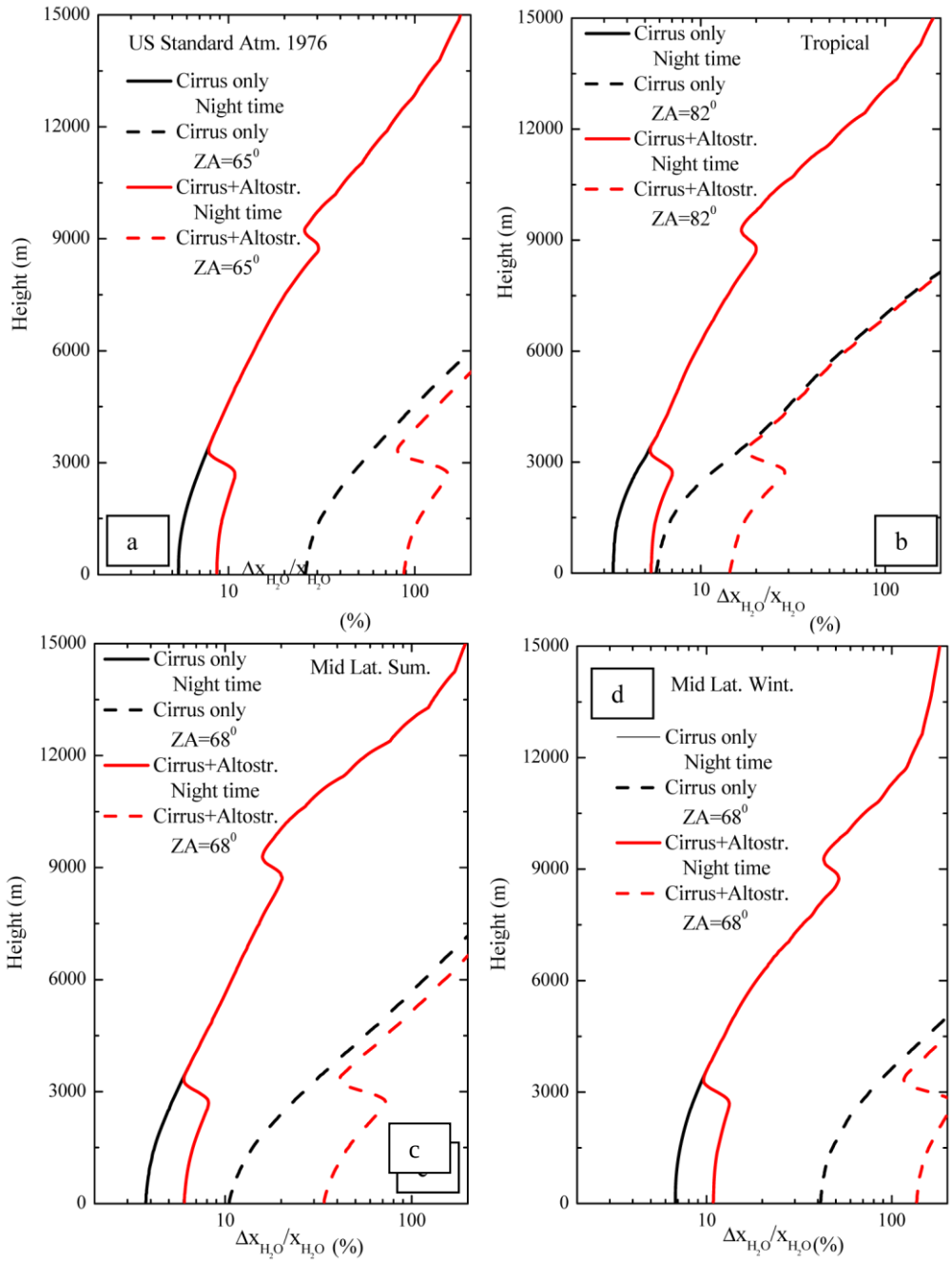


Fig. 8. Vertical profiles of $\Delta x_{H_2O}(z)/x_{H_2O}(z)$ in cloudy conditions for the US Standard Atmosphere 1976 (panel a), the Tropical (panel b) and Mid-Latitude Summer/Winter atmospheric reference models (panel c and d, respectively). In the figure, two scenarios are considered: the presence of the cirrus cloud only and the presence of both the cirrus and the mid-level cloud. Simulations in this figure consider a horizontal resolution of 50 km.

Optics EXPRESS

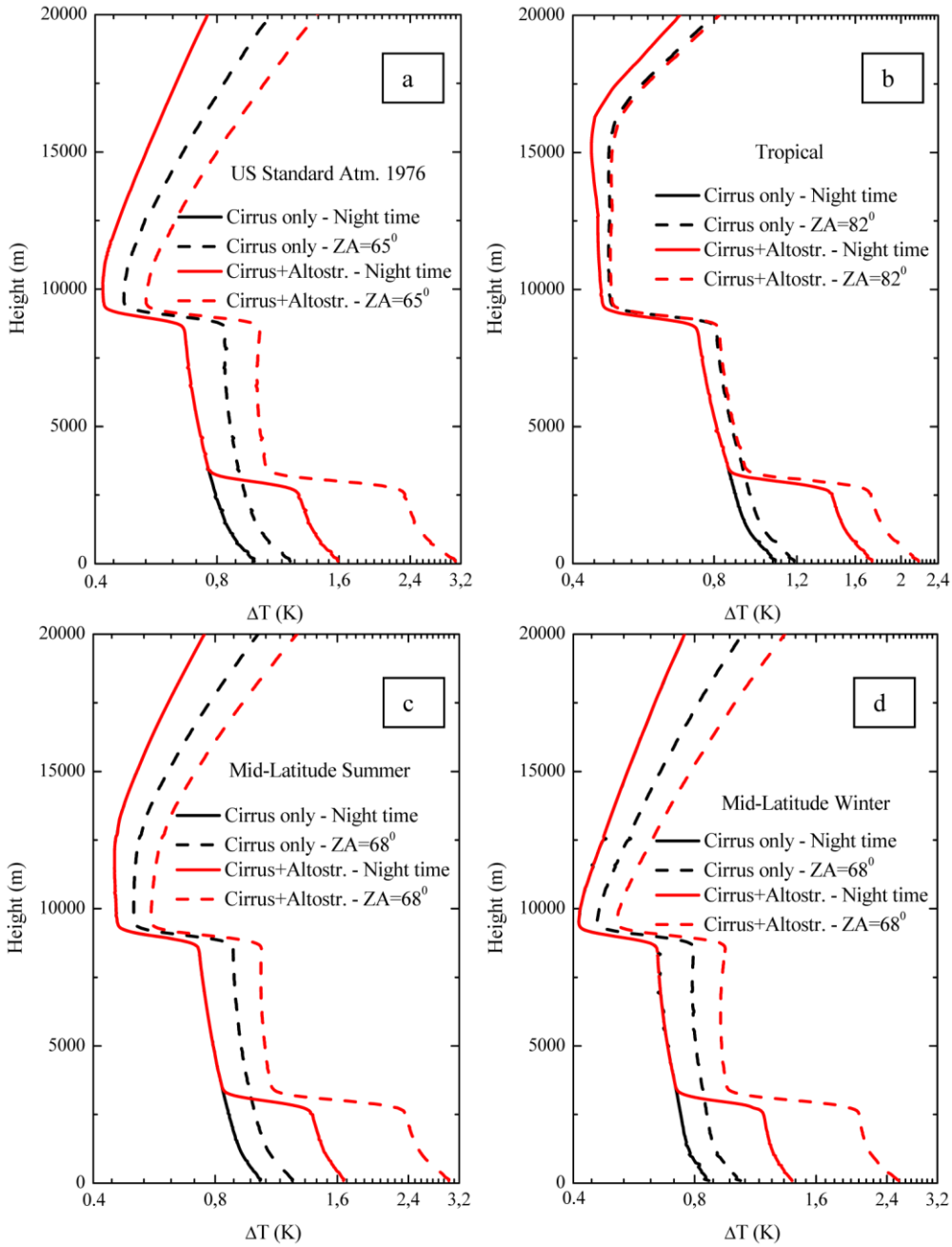


Fig. 9. Vertical profiles of $\Delta T$ in cloudy conditions for the US Standard Atmosphere 1976(panel a), the Tropical (panel b) and Mid-Latitude Summer/Winter atmospheric reference models (panel c and d, respectively). In the figure, two scenarios are considered: the presence of the cirrus cloud only and the presence of both the cirrus and the mid-level cloud. Simulations in this figure consider a horizontal resolution of 50 km.

## 6. Summary and final remarks

In the present paper the performance of a space-borne water vapour and temperature Raman lidar has been simulated. We have reported simulations under a variety of climate scenarios, demonstrating the capability of a space-borne Raman lidar to provide global-scale water

vapour and temperature measurements throughout the troposphere, with a major impact from the surface to the lower troposphere. Simulations have been performed based on the application of an analytical model developed by Di Girolamo *et al.* (2006) [16], properly modified for the purposes of the present research effort. Simulation results demonstrate that a space-borne Raman lidar system exploiting the vibrational and pure rotational Raman techniques in the UV and taking advantage from state-of-the-art transmitter–receiver technology is capable to perform day- and night-time atmospheric water vapour mixing ratio and temperature measurements in cloud-free conditions with an accuracy fulfilling observational requirements for NWP and most climate research applications, from the surface to the lower troposphere, with especially high performance in the PBL, with vertical and horizontal resolutions of 200 m and 50 km, respectively. Therefore, the availability of such a data set would strongly impact next-generation regional and global atmospheric models used for weather forecast and climate trend studies, and could be used for the verification of Earth system models (e.g. the assessment of model errors and biases, i.e. www.gruan.org,www.gaia-clim.eu), for the calibration of space-borne passive remote sensing systems, and for convective-scale data assimilation efforts and various process studies, with a strong potential impact on our understanding and predictive capabilities of the water and energy cycles of the Earth system, including extreme events. Additionally, the availability of such a data set would allow closing extremely critical gaps in the characterization of the land-atmosphere system up to 3 km, with an extraordinary high vertical resolution, even allowing to determine the PBL depth directly and globally using the temperature profile measurements. Only with a system like this deployed in space, the current "terra incognita" in Earth observation, namely the thermodynamic profiles in the PBL, can be explored. In this respect, it is also worthwhile mentioning that passive remote sensing systems do not have the potential to come even close to this performance due to the intrinsic limitations in the inversion with respect to height of the radiative transfer equation [10]. An additional advantage of the proposed system when compared with passive remote sensing systems is the detailed characterization of the measurement uncertainty at each altitude and for each individual profile, obtained through the application of Poisson statistics to the detected signal photons, which results in a strong positive impact on numerical weather prediction, fully exploiting the potential of the measured profiles in weather forecast models through data assimilation [73]. Simulations also reveal that NWP and climate research observational requirements can also be fulfilled above and below thin cirrus-like clouds with an optical thickness of 0.3.

The impact of a space mission based on this concept on weather and climate research can be further enhanced by exploiting synergies with passive instruments on other space platforms, such as IASI-A/B, CrIS and AIRS [87, 88] and GNSS occultation. Synergy exploitation strategies primarily benefit from the high vertical resolution of lidar measurements and the large coverage and high horizontal resolution of these passive sensors [10,85].

System performances could be further improved with respect to those reported in the present paper based on a further refinement of specific system technical characteristics. In this respect it is to be specified that a consolidated value for the receiver FOV of 25 μrad, already implemented in other space lidar systems [89, 90], was considered in the reported simulations. Preliminary feasibility assessments carried out by space companies in the frame of the technological studies in support of this instrumental concept led to the conclusion that the achievable mechanical stability within the platform is sufficiently high to obtain a pointing stability level for both the transmitter and the receiver allowing to make a 10 μrad FOV technologically feasible.

It should be finally noticed that several studies on large-aperture mirrors (20–30 m diameter) have been funded by NASA [91–93] and are currently considered for prototyping, while the feasibility of space-qualified 100–400 W power laser sources for lidar applications

Optics EXPRESS

is currently under investigation (e.g [55–58]. These technological possibilities open new scenarios in atmospheric thermodynamic monitoring from space.

## Acknowledgments

Authors wish to thank the ATLAS team members for the fruitful discussion in the frame of ESA EE-9, Revised EE-9 and EE-10 Calls finalized to the definition of the mission observational requirements and concept.